JGR Solid Earth

RESEARCH ARTICLE

10.1029/2023JB027299

Key Points:

- Teleseismic P attenuation is largely anti-correlated with upper mantle seismic velocity
- Significant lateral variations in attenuation are observed in the tectonically quiescent regions
- The ratio of attenuation to velocity anomaly amplitudes may be indicative of mantle conditions

Supporting Information:

Supporting Information may be found in the online version of this article.

Correspondence to:

M. J. Bezada,
mbezada@umn.edu

Citation:

Bezada, M. J., Byrnes, J. S., Zhu, Z., & Lee, H. (2023). Lateral variations in teleseismic attenuation of the conterminous U.S. and new insights derived from its relationship to Mantle seismic velocity. *Journal of Geophysical Research: Solid Earth*, *128*, e2023JB027299. https://doi.org/10.1029/2023JB027299

Received 21 JUN 2023
Accepted 22 NOV 2023

Author Contributions:

Conceptualization: M. J. Bezada, J. S. Byrnes
Formal analysis: M. J. Bezada, J. S. Byrnes, Z. Zhu, H. Lee
Methodology: M. J. Bezada, J. S. Byrnes
Software: M. J. Bezada, J. S. Byrnes
Supervision: M. J. Bezada
Visualization: M. J. Bezada
Writing – original draft: M. J. Bezada
Writing – review & editing: J. S. Byrnes, Z. Zhu, H. Lee

© 2023. The Authors.
This is an open access article under the terms of the Creative Commons Attribution-NonCommercial-NoDerivs License, which permits use and distribution in any medium, provided the original work is properly cited, the use is non-commercial and no modifications or adaptations are made.

Lateral Variations in Teleseismic Attenuation of the Conterminous U.S. and New Insights Derived From Its Relationship to Mantle Seismic Velocity

M. J. Bezada[1], J. S. Byrnes[2], Z. Zhu[1], and H. Lee[3]

[1]University of Minnesota, Twin Cities, Minneapolis, MN, USA, [2]Northern Arizona University, Flagstaff, AZ, USA, [3]Seoul National University, Seoul, Republic of Korea

Abstract

Much of our knowledge of the North American lithosphere comes from imaging seismic velocities. Additional constraints on the subsurface can be gained by studying seismic attenuation, which has different sensitivity to physical properties. We produce a model of lateral variations in attenuation across the conterminous U.S. by analyzing data recorded by the EarthScope Transportable Array. We divide the study area into 12 overlapping tiles and differential attenuation is measured in each tile independently; and twice for four of the tiles. Measurements are combined into a smooth map using a set of linear inversions. Comparing results for adjacent tiles and for repeated tiles shows that the imaged features are robust. The final map shows generally higher attenuation west of the Rocky Mountain Front than east of it, with significant small length scale variations superimposed on that broad pattern. In general, there is a strong anticorrelation between differential attenuation and shear wave velocities at depths of 80–250 km. However, a given change in velocity may correspond to a large or small change in attenuation, depending on the area; suggesting that different physical mechanisms are operating. In the western and south-central U.S., as well as the Appalachians, velocity variations are large compared to attenuation changes, while the opposite is true in the north-central and southeastern U.S. Calculations with the Very Broadband Rheology calculator show that these results are consistent with the main source of heterogeneity being temperature and melt fraction in the former regions and grain size variability in the latter ones.

Plain Language Summary

Seismic waves in the mantle propagate at lower speeds when temperatures are higher, rocks have higher water content, and small amounts of melt are present. These conditions also affect how much energy the wave loses as it passes through, which we call seismic attenuation. In this study we produce a map of seismic attenuation for the conterminous United States. We find that, in most places, where seismic velocities are low, attenuation is high, and vice versa. This is what we expect. Interestingly, the size of the change in attenuation that corresponds to a given change in velocity varies by region. In places with thicker lithosphere and without recent tectonic activity attenuation anomalies are large compared to velocity anomalies, the opposite is true in places with thin lithosphere and recent tectonic activity. Considering the results of lab experiments on velocity and attenuation, this suggests that in the regions with thick lithosphere and without recent tectonic activity the main cause of the anomalies is changes in the size of the mineral grains in the mantle, whereas in the regions with thin lithosphere and recent tectonic activity the main cause of the anomalies is changes in temperature and the amount of melt.

1. Introduction

Like all continents, North America is an amalgamation of lithospheric terranes of different ages, origins and characteristics that has been assembled around a cratonic core over billions of years (e.g., Whitmeyer & Karlstrom, 2007). The conterminous United States constitutes a large fraction of the North American continent and seismic data acquired by the EarthScope Transportable Array (TA) provided unprecedented data coverage of this region. The result has been the development of models of seismic properties with much higher resolution than previously possible, including the seismic characterization of the lithosphere-asthenosphere system at a continental scale in unprecedented detail. One of the more impactful legacies of the EarthScope initiative is the discovery of complexity and heterogeneity in the "stable" continental lithosphere east of the Rocky Mountains, far from any plate boundary regions.

Most products of the TA characterize the propagation velocity of seismic waves, whether through the constraint of absolute velocities, velocity anomalies, velocity contrasts, or velocity anisotropy (e.g., Buehler & Shearer, 2017; Hopper & Fischer, 2018; Lin & Schmandt, 2014; Porritt et al., 2021; R. Porter et al., 2016; Schmandt & Lin, 2014; Shen & Ritzwoller, 2016; Zhou et al., 2022). An additional and complementary observable is seismic attenuation. Attenuation has different and less well-understood sensitivity to the variables that describe the physical state of the subsurface (e.g., temperature, composition, and melt content). Typically, variations in physical properties that reduce seismic velocity increase attenuation, but some properties have a greater impact on attenuation than velocity, while the inverse is true for others (e.g., Havlin et al., 2021). Therefore, a joint interpretation of attenuation and velocity can reduce the ambiguity that is inherent in the interpretation of seismic velocity structure alone. In contrast to the abundance of studies of seismic velocity of the North American lithosphere-asthenosphere system, studies of attenuation are scarce and often come with significant caveats. The model of Lawrence et al. (2006) predates the TA and has strong features that are hard to correlate to known geologic structure. The Cafferky and Schmandt (2015) model represents the state of the art for body wave attenuation, but the authors caution that it is difficult to establish the correct amount of smoothing for their data and that scattering, rather than attenuation, may be a strong driver of their results. A Rayleigh wave based study of attenuation by Bao et al. (2016) produced a model with much short wavelength variation that is difficult to interpret without substantial ad-hoc smoothing and the authors caution that their correction for the focusing and defocusing of the wavefield may not be accurate for the degree of heterogeneity in the conterminous United States.

In this study, we perform a time-domain analysis of direct *P* waveforms from deep earthquakes recorded by the TA stations to measure relative attenuation, and combine those measurements into a two-dimensional model for the conterminous U.S. As expected, we find attenuation is generally higher west of the Rocky Mountain Front (RMF), but only to first order. Larger than expected changes in attenuation occur east of the RMF. Many of the attenuation anomalies correlate well with velocity anomalies but the proportionality between velocity and attenuation differs substantially in different regions, meaning a given change in velocity can correspond to either a small or large change in relative attenuation in different places. This observation suggests that the dominant source of heterogeneity in different parts of the study area are lateral variations in different mantle state variables: temperature and melt fraction for young, thin lithosphere and grain size for old, cold lithosphere.

2. Data and Methods

We apply attenuation measurement and imaging techniques that have been successfully used recently in different settings (Bezada, 2017; Bezada & Smale, 2019; J. S. Byrnes & Bezada, 2020; J. S. Byrnes et al., 2019; Deng et al., 2021; Zhu et al., 2021). We measure t^* in the time domain by numerically attenuating an estimate of the source time function to match the observed waveforms. The individual t^* measurements are used to invert for a background attenuation field plus station and event terms. Compared to previous studies, the scale of the study area warrants the use of different strategies for data analysis and inversion for a smooth map, which we describe below.

2.1. General Approach

The goal of the study is to image lateral variation in attenuation over the conterminous United States, an area of ~8 million km^2 covered by the nearly 1800 stations of the TA in a ~70 km spaced grid (Figure 1). To measure differential attenuation (Δt^*) we use the time domain method of Bezada (2017), which is based on the work of Adams and Humphreys (2010). The least attenuated traces (as determined visually by the analyst) are stacked to produce an estimate of the source-time function and this estimate is numerically attenuated over a range of Δt^* to generate synthetic waveforms with different degrees of attenuation. The synthetics that best-fit the observed waveforms thus provide an estimate of Δt^*. Note that the absolute degree of attenuation in the initial estimated source-time function is not known and so only relative values can be constrained.

Two confounding factors are particularly relevant to this study. The first is directivity, which produces systematic variations in the width of the waveform with azimuth. This poses a challenge when applying the waveform matching approach over too large of an area because broadening of the waveforms by directivity may be misinterpreted as broadening of the waveforms by attenuation. Previous studies ignored directivity because the backazimuth is nearly constant for a small study area (Bezada, 2017; J. S. Byrnes & Bezada, 2020; J. S. Byrnes et al., 2019; Zhu

21699356, 2023, 12, Downloaded from https://agupubs.onlinelibrary.wiley.com/doi/10.1029/2023JB027299, Wiley Online Library on [11/12/2023]. See the Terms and Conditions (https://onlinelibrary.wiley.com/terms-and-conditions) on Wiley Online Library for rules of use; OA articles are governed by the applicable Creative Commons License

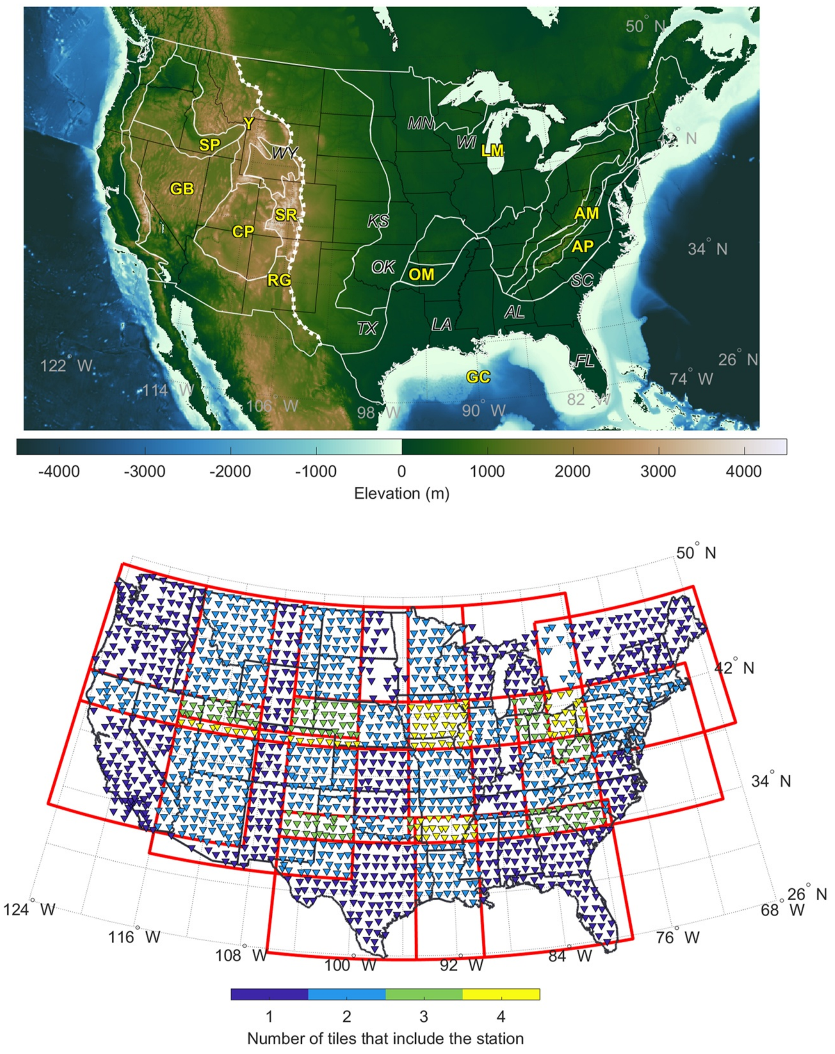

Figure 1. (Top) Topographic map of the study area with state boundaries and tectonic boundaries. The Rocky Mountain Front is indicated by a thick dashed line. Tectonic provinces and other geographic features mentioned in the text are labeled in yellow letters: Y, Yellowstone; SP, Snake River Plain; GB, Great Basin; CP, Colorado Plateau; SR, Southern Rocky Mountains; RG, Rio Grande Rift; GC, Gulf Coast; OM, Ouachita Mountains; LM, Lake Michigan; AM, Appalachian Mountains; AP, Appalachian Piedmont. States mentioned in the text are labeled in italics: WY, Wyoming; KS, Kansas; OK, Oklahoma; TX, Texas; MN, Minnesota; WI, Wisconsin; LA, Louisiana; AL, Alabama; SC, South Carolina; FL, Florida. Bottom: Spatial distribution of seismic stations used in this study (inverted triangles) and limits of the "tiles" into which the study area was divided (red lines). Seismic stations are color-coded according to the number of tiles in which they are included. Only stations that yielded Δt^* measurements are shown.

et al., 2021). However, this assumption is less valid when the method is applied at this spatial scale. A second confounding factor is the reliance on the analyst to identify which traces to include in the estimate of the unattenuated source-time function, and in quality control to accept or reject measurements based on the quality of the fit to the observed waveforms. These aspects could make the results subjective and raise questions on the dependence of the final model on choices made by individual analysts.

To address both of these challenges, we divide the study region into 12 overlapping tiles (Figure 1). Each tile generally encompasses 9.5 degrees of latitude by 16 degrees of longitude and has varying amounts of overlap with adjacent tiles (Figure 1). The locations of the tiles were chosen in an ad-hoc manner to conform to irregularities in the shape of the array which result from national borders as well as the Atlantic and Gulf of Mexico coasts. For the same reason, some tile sizes deviate from the nominal 9.5° by 16° dimensions. At the latitudes of the United States, the tile dimensions correspond to a typical maximum angular spread of 12°, in line with the threshold

21699356, 2023, 12, Downloaded from https://agupubs.onlinelibrary.wiley.com/doi/10.1029/2023JB027299, Wiley Online Library on [11/12/2023]. See the Terms and Conditions (https://onlinelibrary.wiley.com/terms-and-conditions) on Wiley Online Library for rules of use; OA articles are governed by the applicable Creative Commons License

estimated by Liang et al. (2022) for isolating in-the-box effects from global structure in teleseismic tomography. Specific tile coordinates are listed in Table S1 in Supporting Information S1. The overlap between the tiles allows us to check for consistency between results at adjacent tiles processed by different analysts. Additionally, we choose four tiles for which the attenuation measurements are done by two different analysts; allowing for a direct comparison and assessment of how the final result depends on analyst choices. In total, 16 tiles are analyzed (12 individual tiles plus 4 repeats), with each of the 4 authors completing the analysis for 4 tiles.

2.2. Stations and Events

In order to maintain even coverage across the study area we analyze data from the TA and the Southern California network but exclude FlexArray deployments. This results in a total of 1,745 stations across the conterminous U.S. with a station spacing of ∼70 km (Figure 1). The number of stations within each tile is variable, ranging from ∼200 to ∼300. Most stations are included in more than 1 tile (Figure 1), with 44%, 8%, and 5% being included in 2, 3, and 4 tiles, respectively. We utilize the vertical component velocity seismograms for measuring attenuation.

As in previous studies, we restrict events to those with hypocentral depths larger than 250 km. These events occur below the low-Q asthenosphere, and so are primarily attenuated on the receiver side, which helps justify the assumption that, for each event, source-side attenuation is common to all receivers. Moreover, deeper events typically have impulsive sources which makes them easier targets for waveform matching. Since we are using teleseismic direct P phases, we restrict the epicentral distances to 30–90 degrees from the center of each tile. Tiles in the west coast are in range of the more seismically prolific subduction zones and thus more earthquakes fitting our criteria are recorded there than in the tiles further east. In order to ensure suitable signal-to-noise ratios only events with moment magnitude >5.5 are examined. In total, the number of events matching the criteria for each tile range from 20 to over 100. Of these, the number of events that yielded useful Δt^* measurements in the different tiles ranges from 10 to >50. Origin times and hypocentral parameters of the events used for each tile are listed in Table S2.

2.3. Measurement of Δt^*

As mentioned in Section 2.1, we utilize the time domain Δt^* measurement method described in Bezada (2017). This method has been shown to be more robust than the traditional spectral ratio method of Teng (1968) (Bezada et al., 2019; J. S. Byrnes & Bezada, 2020). For each event, we produce an estimate of the unattenuated source waveform by selecting and stacking the traces with the most impulsive first arrivals. We find Δt^* for each recorded trace by comparing it with a numerically attenuated version of the estimated source waveform calculated with the attenuation operator of Azimi et al. (1968) in the frequency domain:

$$A = \exp\left\{-\omega \Delta t^* \left[\frac{1}{2} + \frac{i}{\pi}\ln\left(\frac{\omega}{\omega_0}\right)\right]\right\} \tag{1}$$

where ω and ω_0 are the angular frequency and a reference agular frequency, respectively, and only the differential attenuation Δt^* affects the shape of the waveform. We grid-search over Δt^* values and choose the value that minimizes the L2 norm of the misfit between the numerically attenuated source trace and the observed waveform in a selected time window (Figure 2). Inspection of an ensemble of misfit curves suggests that the uncertainty in each Δt^* determination is on the order of 0.07–0.1 s (Text S1 and Figure S1 in Supporting Information S1). The best-fitting synthetic waveform is visually inspected before accepting the Δt^* measurement.

Our procedure does not make any considerations for the frequency dependence of attenuation. Although a small frequency dependence is well documented in experiments (e.g., Jackson & Faul, 2010), the effect is small over the limited bandwidth of our data (0.2–1 Hz). Studies that have attempted to constrain frequency dependence of teleseismic body wave attenuation have shown that the results are nearly identical to those obtained assuming frequency independence (Cafferky & Schmandt, 2015; Eilon & Abers, 2017).

2.4. Construction of the Map

The measurements of Δt^* for any one event can show substantial scatter superimposed on the regional features (Figure 2), and the information from all the events needs to be combined to produce a robust map of lateral

21699356, 2023, 12, Downloaded from https://agupubs.onlinelibrary.wiley.com/doi/10.1029/2023JB027299, Wiley Online Library on [11/12/2023]. See the Terms and Conditions (https://onlinelibrary.wiley.com/terms-and-conditions) on Wiley Online Library for rules of use; OA articles are governed by the applicable Creative Commons License

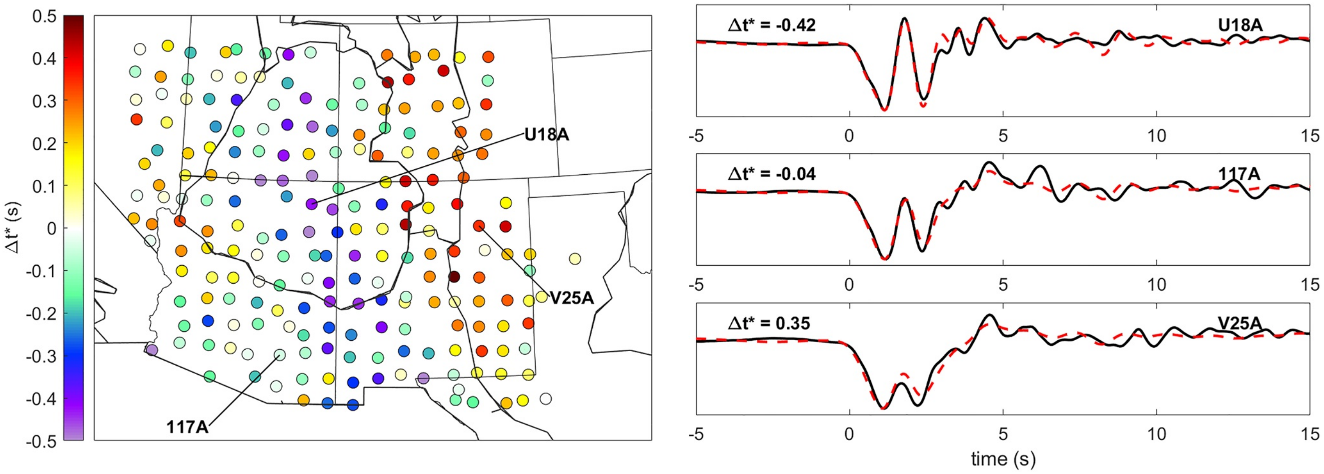

Figure 2. Δ*t** measurements from one event recorded on tile B2 (encompassing the Colorado Plateau and its surroundings) along with example observed (black) and best-fit synthetic (dashed red) waveforms. Waveform panels include the measured value (in seconds) and the station name. Stations for which the waveforms are shown are indicated on the map.

variations in attenuation. We note that, ideally, the Δ*t** measurements could serve as input to a tomographic inversion that solves for variations in the quality factor (Q) not only laterally but also in depth. This is possible when the ray coverage is sufficiently dense, such as when using Wadati-Benioff seismicity beneath the mantle wedge (e.g., Wei & Wiens, 2018, 2020) or when the station spacing is very small (~10 km in J. S. Byrnes & Bezada, 2020). Although the TA provides excellent station density for teleseismic body wave velocity tomography, the restriction to deep earthquakes when measuring attenuation greatly reduces the number and backazimuthal richness of useable events, making Q tomography substantially more challenging. Given this difficulty, one alternative is to calculate the mean Δ*t** for each station and smooth the result (e.g., as in Cafferky & Schmandt, 2015). In contrast, in our previous studies we have adopted two different approaches. The first one is a linear inversion that assumes each measurement is the sum of a smoothly varying background attenuation field, station terms and event terms, and solves for these three components (Bezada, 2017; Bezada & Smale, 2019). The second one is a transdimensional Markov Chain Monte Carlo (TDMCMC) inversion that seeks a set of Voronoi cell models that fit the observations to an appropriate level (J. S. Byrnes et al., 2019; Deng et al., 2021; Zhu et al., 2021). The TDMCMC inversion is especially useful when station coverage is uneven because, having no set node spacing, the model parameterization (and thus its nominal resolution) emerges from the data coverage. For this study, this advantage is not important because station coverage is even across the study area, and the linear inversion is thus suitable. An advantage of the linear inversion is that it includes station terms that can absorb the effect of local structure or site effects. One could add station terms to the Bayesian inversion, but here this would add on the order of 1,800 additional unknowns to the problem, making it computationally intractable. A preliminary Bayesian inversion of the data set (without station terms) produced a map with abundant small-wavelength anomalies, many of them encircling a single station (Figure S2, associated uncertainties in Figure S3 in Supporting Information S1). For this reason, we prefer to use a linear inversion scheme for this data set.

The challenge with a linear inversion is selecting the optimal set of regularization parameters and characterizing the uncertainty. We implement an inversion that includes advantages from both of the previously used methods in that each individual inversion is linear as described in Bezada (2017), but many inversions are performed, and the optimal regularization parameters are found through a Bayesian scheme following the formalism of Malinverno and Briggs (2004). The final model is made by averaging all the accepted linear inversion results, and taking the standard deviation at each point provides an idea of the uncertainty related to regularization parameters. For more details on the method see Text S2 in Supporting Information S1.

An important question around using the inversion approach when applied to this data set is if large east-west oriented gradients can be resolved. This is not only because of our division of the study area into tiles for data analysis, but because of the deployment strategy of the TA, which consisted in an eastward rolling north-south oriented band of receivers. We de-mean our *t** measurements for each event as recorded in each tile, and rely on the event terms to accurately recover structure spanning more than one tile, or more than one band of receivers.

21699356, 2023, 12, Downloaded from https://agupubs.onlinelibrary.wiley.com/doi/10.1029/2023JB027299, Wiley Online Library on [11/12/2023]. See the Terms and Conditions (https://onlinelibrary.wiley.com/terms-and-conditions) on Wiley Online Library for rules of use; OA articles are governed by the applicable Creative Commons License

10.1029/2023JB027299

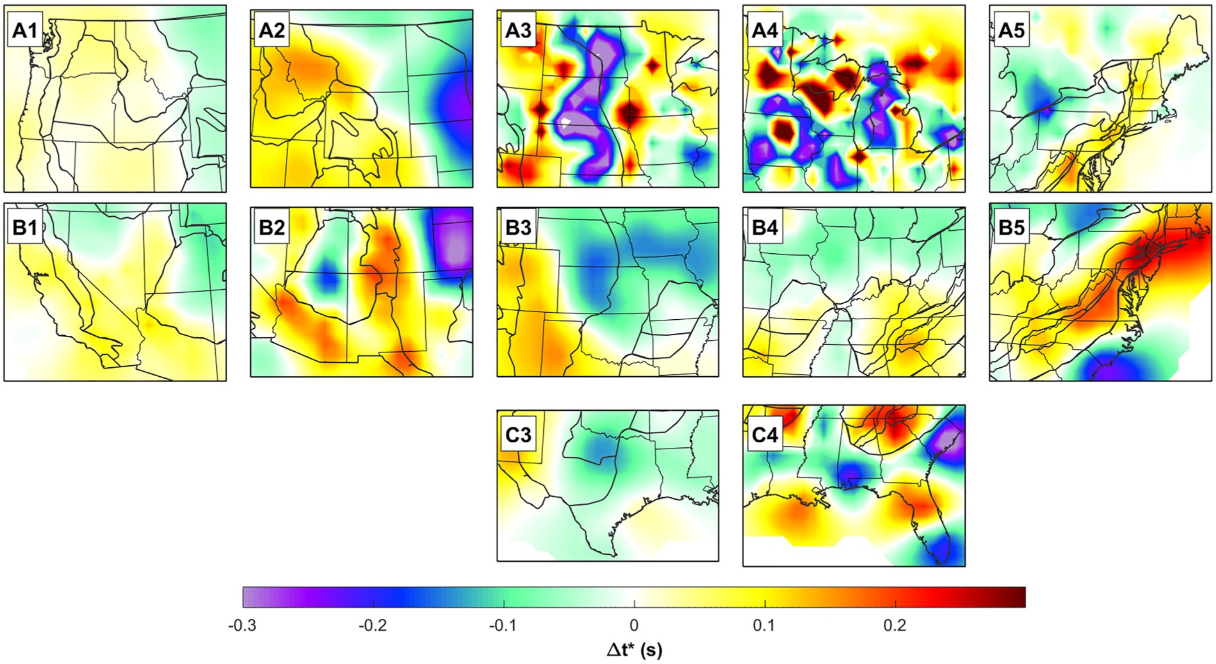

Figure 3. Δ*t** maps resulting from the inversion of data from each individual tile separately. Thinner black lines show state boundaries, thicker black lines show tectonic province boundaries. Panels are arranged according to their geographic location of the tile they represent. Tile names are indicated in the upper left corner of each panel.

To verify that the inversion performs as intended, we conduct a synthetic test where we attempt to recover two continent-spanning horizontal gradients in attenuation (see details in Text S3 in Supporting Information S1). The output model accurately reproduces the input from the synthetic data, verifying the adequacy of our strategy (Figures S4 and S5 in Supporting Information S1).

3. Attenuation Model

We present our results in three parts. First, we run the inversion procedure for each tile individually. We then show the results obtained by different analysts for specific tiles. Finally, we obtain the full model by running the inversion for the entire data set consisting of the Δ*t** measurements from all the tiles.

3.1. Individual Tiles

Results for each of the individual tiles show that the algorithm finds different regularization parameters for each tile which is reflected in the amplitude and roughness of the anomalies. Broadly speaking, the algorithm will prefer sharper and higher amplitude features when the Δ*t** values are more internally consistent. We note that the two tiles with the roughest results (A3 and A4 in Figure 3) were processed by different analysts and there is no obvious relationship between the analyst and the roughness of the result. Importantly, patterns of low and high attenuation on the edges of the tiles (where there is overlap) are consistent between adjacent tiles (Figure 3). As a measure of this consistency, we calculate the correlation coefficient between Δ*t** values for the overlapping sections as determined from the inversion of the measurements in two neighboring tiles. The average correlation coefficient is 0.68 with a standard deviation of 0.17. Methodological details and cross-correlation coefficient values for each pair of adjacent tiles are included in Text S4, Figure S6 in Supporting Information S1. Tiles where the analysis was done independently by two different analysts also show consistent results (Figure 4), with the main difference being the amplitude and roughness of the anomalies, again reflecting differences in regularization. The average correlation coefficient between Δ*t** values obtained by two different analysts for the same tile is 0.77. Spatial patterns of high and low attenuation seem thus to be robustly constrained by our analysis. We perform this exercise primarily to check for consistency, and consider the inversion of the ensemble data set the preferred model.

21699356, 2023, 12, Downloaded from https://agupubs.onlinelibrary.wiley.com/doi/10.1029/2023JB027299, Wiley Online Library on [11/12/2023]. See the Terms and Conditions (https://onlinelibrary.wiley.com/terms-and-conditions) on Wiley Online Library for rules of use; OA articles are governed by the applicable Creative Commons License

21699356, 2023, 12, Downloaded from https://agupubs.onlinelibrary.wiley.com/doi/10.1029/2023JB027299, Wiley Online Library on [11/12/2023]. See the Terms and Conditions (https://onlinelibrary.wiley.com/terms-and-conditions) on Wiley Online Library for rules of use; OA articles are governed by the applicable Creative Commons License

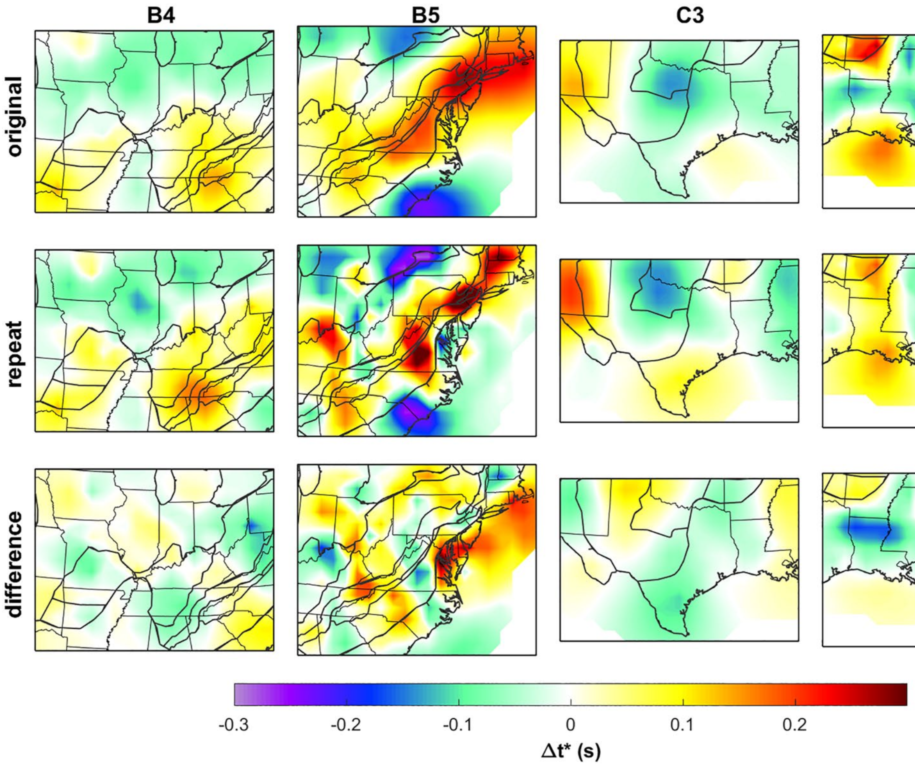

Figure 4. Comparison of Δ*t** maps resulting from the inversion of data from each of the 4 tiles that were processed independently by two different analysts. The top and middle rows correspond to results from inverting the measurements made by the first and second analyst, respectively. The bottom row shows the difference between the two models. Tile names are indicated above each column. Note that for all tiles spatial patterns of low and high attenuation are consistent in the two independent analyses. Thinner black lines show state boundaries, thicker black lines show tectonic province boundaries.

3.2. Complete Model

We now present the result of inverting the data from all the tiles shown in Figure 3 together. The entire study region shows a range in Δ*t** of roughly −0.25 to 0.25 s and, to first order, results broadly conform to the expectation of higher attenuation west of the RMF (Figure 5). However, low attenuation anomalies are found in the western U.S. and high-attenuation anomalies are found in the central and eastern U.S. (Figure 5). We note that the general patterns and indeed many of the smaller-scale features in our model are consistent with the attenuation model of Cafferky and Schmandt (2015). For their model using a smoothing radius of 1.75° (see their Figure 4b), the correlation coefficient between the two models is 0.75.

West of the RMF, we observe mostly high attenuation with a mean Δ*t** value of 0.08 s and a standard deviation of 0.07 s. Relatively low attenuation (Δ*t**of −0.02 to −0.08 s) is observed in the core of the Colorado Plateau (CP) and further north in SW Wyoming (Figure 5). High attenuation values surround the CP on the remaining three sides (to the west, east and south) with the southern Rocky Mountains directly east of the CP showing some of the highest attenuation values in the whole model (Δ*t** of up to 0.22 s). The central and NW great basin show average to slightly positive differential attenuation (Δ*t** as low as 0.02 s). The NW U.S. (west of the RMF and north of ~43°N) shows moderately high attenuation (~0.1 s) with some small fluctuations. Surprisingly, given the very low seismic velocities widely documented in this region (e.g., Schmandt & Lin, 2014; Shen & Ritzwoller, 2016; Stanciu & Humphreys, 2020), the eastern Snake River Plain (SRP) and the Yellowstone area do not feature high attenuation, and the area is unremarkable in the attenuation map (Figure 5). In this model, we do not observe a clear low-attenuation region that one would expect to be associated with the Juan de Fuca slab. Directly south of ~39°N where tomography models place the southern end of the slab (e.g., Bodmer et al., 2018; Hawley et al., 2016; Schmandt & Lin, 2014), our model shows a very high attenuation anomaly (Δ*t** of 0.18–0.24 s, Figure 5).

East of the RMF, attenuation is remarkably heterogenous. We find alternating high and low attenuation anomalies with length scales on the order of ~200 to ~1,000 km. A notable 200–300 km wide low-attenuation

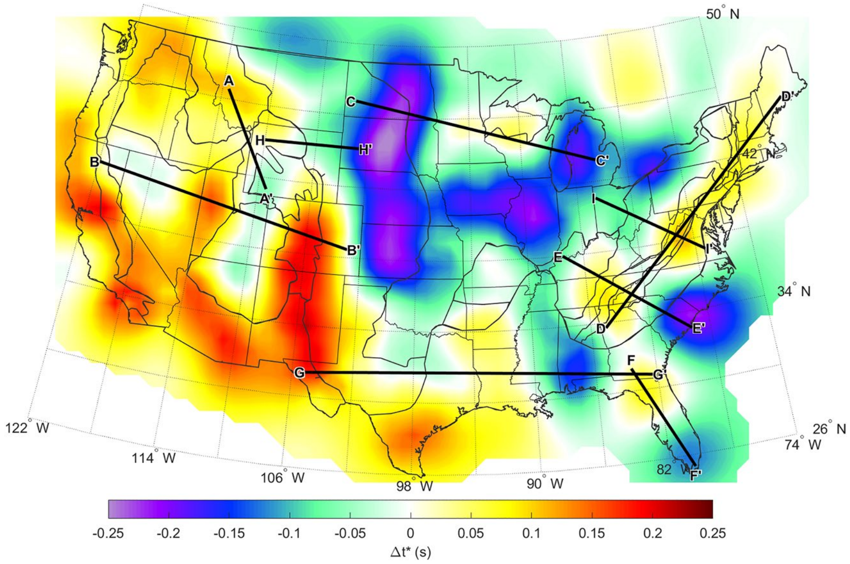

Figure 5. Δ*t** map resulting from the inversion of the entire set of measurements. Thinner black lines show state boundaries, thicker black lines show tectonic province boundaries. Also indicated in the figure are the locations of the profiles shown in Figure 10. Uncertainties associated with regularization are shown in Figure S7 in Supporting Information S1.

anomaly (Δ*t** of −0.14 to −0.26 s) extends roughly N-S from the northern end of the model at 50° N to near the Oklahoma-Kansas border at ∼36.5°N (Figure 5). East of this anomaly, relatively high attenuation is observed at 44°–47°N with peaks that reach Δ*t** values of 0.08 s over the states of Minnesota and Wisconsin and a local minimum between these attenuation peaks that coincides with the axis of the mid-continent rift. Attenuation is again low east of Lake Michigan (as low as −0.18 s). Attenuation is also low directly south of the Minnesota-Wisconsin anomalies and further south the model shows mildly negative to neutral attenuation; with the exception of positive attenuation anomalies (0.05–0.15 s) beneath the Texas and Louisiana Gulf Coast and continuing north into the Ouachita Mountains (Figure 5).

In the eastern U.S., the Appalachians are characterized by a band of moderately high attenuation (comparable to values in the NW U.S.) punctuated by three local maxima in the southern, central, and northern Appalachians where Δ*t** values are as high as 0.14 s. A very low attenuation block (with some of the lowest values in the entire model, Δ*t** of −0.18 to −0.3 s) is seen east of the Appalachian piedmont in South Carolina. Significantly low attenuation is also observed in southern Florida, south of ∼27.5°N and in the central Gulf Coast between 86° and 88°W, in both cases reaching a minimum value of −0.18 s.

3.2.1. Synthetic Recovery Test

As stated above, the expected anomalies associated with the eastern SRP and the Juan de Fuca slab are absent from our attenuation model. To investigate to what degree this is simply a resolution issue, we conduct another synthetic test. In this case, the input model is the output of our inversion with the amplitudes increased by a factor of 1.1 (as a first order attempt to counteract the damping effect of regularization) on which we superimpose low and high attenuation anomalies representing the Juan de Fuca slab and the eastern SRP, respectively. The geometry of the anomalies is guided by the velocity model of Schmandt and Lin (2014). The results suggest that the SRP and, to a lesser extent, the Juan de Fuca slab should be partially recovered (Figures S8 and S9 in Supporting Information S1). In the case of the Juan de Fuca slab, one potential reason for our model not recovering it as well as would be expected from the synthetic test is the tradeoff between the presumably low-attenuation slab and the presumably high-attenuation mantle wedge (see Deng et al., 2021 for a discussion). The effects of these two likely anomalies would tend to cancel each other out. Another potential reason is multipathing or focusing effects. Pang et al. (2023) use full wave propagation simulations to show that these effects can mimic attenuation. The simulated S waves in that study had dominant periods of 20 s, which corresponds to wavelengths in the uppermost mantle on the order of 80 km. In contrast, *P* waves used in this study have dominant frequencies of ∼1 hz, corresponding to wavelengths of ∼8 km. The order of magnitude difference in wavelength makes it unlikely that the

21699356, 2023, 12, Downloaded from https://agupubs.onlinelibrary.wiley.com/doi/10.1029/2023JB027299, Wiley Online Library on [11/12/2023]. See the Terms and Conditions (https://onlinelibrary.wiley.com/terms-and-conditions) on Wiley Online Library for rules of use; OA articles are governed by the applicable Creative Commons License

same focusing effects would be observed, as J. S. Byrnes et al. (2019) demonstrated that focusing artifacts will average to zero at the length-scale of this study. Additionally, we note that a negative Δt^* anomaly has been observed over the Juan de Fuca slab when applying our method to a denser data set (Oliveira & Bezada, 2022) and that a negative Δt^* anomaly over the subducting slab in southern Alaska has also been imaged with our method and a dense data set (Karayazi, 2022). With regards to the SRP anomaly, the synthetic recovery test strongly suggests that if there was a strong attenuation anomaly there we would partially recover it. Unlike the case of the Juan de Fuca slab, we do not expect there to be a strong low-attenuation anomaly that would cancel the effect of the presumed high attenuation in the SRP, so this is not a likely explanation for our observations. The absence of an attenuation anomaly over the SRP is discussed further in Sections 4.1 and 4.2.1 below.

4. Relationship to Seismic Velocity

Theory and empirical constraints dictate that seismic velocity and quality factor (Q) should correlate, and hence Δt^* should anti-correlate with velocity anomalies. Laboratory experiments have constrained the relationship between velocity and quality factor for changes in temperature and grain size under upper mantle conditions (e.g., Faul & Jackson, 2005; Jackson & Faul, 2010). The effect of melt and volatiles is less well known and still debated, but studies typically predict these factors lead to an anticorrelation between velocity and Δt^* (Chantel et al., 2016; Faul et al., 2004; Yamauchi & Takei, 2016) with some exceptions (Cline et al., 2018; Hammond & Humphreys, 2000). An important caveat is that empirically derived models of the dependence of seismic observables on mantle state variables show that velocity is more sensitive to melt fraction than attenuation, while the opposite is true for grain size (Havlin et al., 2021). For this reason, over a study area as large as ours, where temperature, melt fraction and grain size are likely all varying laterally, one should not expect attenuation and velocity structure to be mirror images of each other. Instead, we expect only a partial anticorrelation between the two seismic properties. In this section we explore how our imaged attenuation anomalies relate to mantle velocity structure.

4.1. Whole Study Area

Seismic velocity models of the conterminous U.S. are abundant, and the similarity between different models suggests the results are robust (e.g., Becker, 2012; Pavlis et al., 2012). We compare our attenuation model to the body wave model of Schmandt and Lin (2014) and the surface-wave model of Shen and Ritzwoller (2016). While velocity models constrain the variations in seismic properties in three dimensions, in Section 2.4 we discuss why it is more difficult to do the same with attenuation. Instead, the differential attenuation measurements we present are path-integrated and thus have no intrinsic control on variations in Q with depth. However, forward calculations show that changes in attenuation due to thermal differences are primarily controlled by mantle conditions in the upper 150–200 km (Soto Castaneda et al., 2021). This is consistent with empirical findings from previous studies that have shown that the anticorrelation between velocity structure and attenuation is strongest at depths of 100–200 km (J. S. Byrnes et al., 2019; H. Liu et al., 2022; Zhu et al., 2021). A correction for physical dispersion due to anelasticity is not made, but would not significantly change the results given the relevant periods (J. Byrnes et al., 2023).

For the attenuation model we present here, we also find a substantial anti-correlation with seismic velocity at depths typical of the lithosphere and asthenosphere (Figure 6). We calculate the correlation coefficient by resampling the two different P and S velocity models at each depth at the locations of grid points in our model. We thus get the correlation coefficient as a function of depth and find a peak value of −0.6 for both P and S velocities with the model of Shen and Ritzwoller (2016) at 120 km depth (near the bottom of their model) and of −0.5 for P and −0.56 for S velocities at a depth of 60 km in the model of Schmandt and Lin (2014). In the case of the Schmandt and Lin (2014) model, the degree of anticorrelation remains at a similar level to depths of 200–300 km and drops for deeper depths (Figure 6a). Considering this, and the fact that Δt^* is a measurement of integrated attenuation, we focus further discussion on comparing our attenuation model with the Schmandt and Lin (2014) model shear wave velocity anomaly (dV_s/V_s) model averaged between depths of 80 and 250 km (Figure 7).

In this depth-averaged velocity model, the highest velocities occur east of the RMF along a roughly NS line, similar to the Δt^* model, although with the edge of the highest-velocity region shifted slightly east (Figure 7). Some internal variation in this high-velocity block in the interior of the continent is observed, including local

21699356, 2023, 12, Downloaded from https://agupubs.onlinelibrary.wiley.com/doi/10.1029/2023JB027299, Wiley Online Library on [11/12/2023]. See the Terms and Conditions (https://onlinelibrary.wiley.com/terms-and-conditions) on Wiley Online Library for rules of use; OA articles are governed by the applicable Creative Commons License

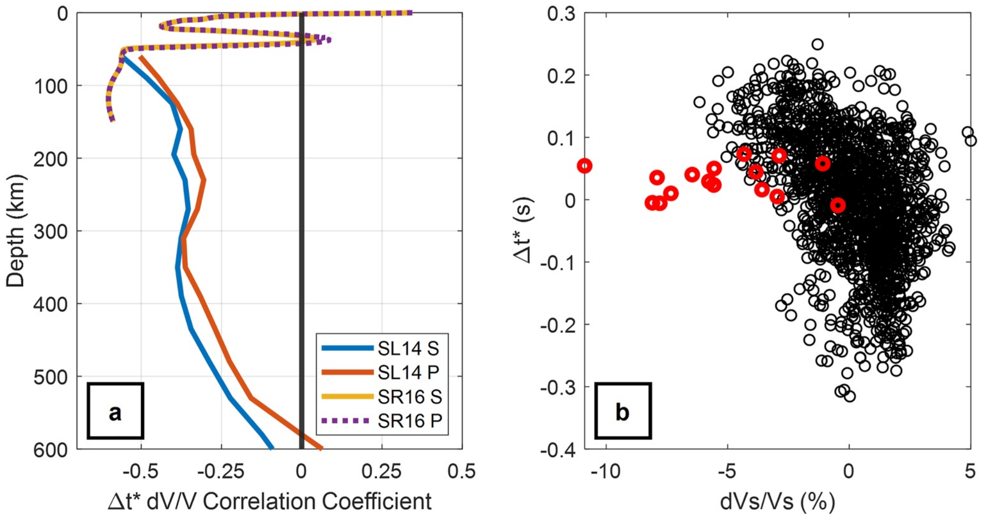

Figure 6. Panel "(a)"—Correlation between our Δt^* map and P and S velocity anomaly values as a function of depth. The different curves represent correlation with the Schmandt and Lin (2014) model (SL14 in the legend) and the Shen and Ritzwoller (2016) model (SR16 in the legend). Panel "(b)" —Scatter plot of Δt^* versus dV_s/V_s at averaged between 80 and 250 km in the model of Schmandt and Lin (2014). Red open circles correspond to model cells in the eastern Snake River Plain, Yellowstone area.

reductions in velocity in central Minnesota, central Wisconsin and central Michigan. The MN and WI anomalies correspond closely to the high attenuation regions we image in the same area, though with weaker relative variations. The western U.S. has generally lower velocities with the lowest being in the Yellowstone-Snake River Plain region, an anomaly that is notably absent from the attenuation map. High-amplitude low velocity anomalies also occur around the rim of the CP. High-velocity anomalies in the western U.S. are seen along the Juan de Fuca slab (beneath the Cascades arc), in the core of the CP and in the central Rockies, as well as in the central Great Basin. Apart from the slab anomalies, corresponding low attenuation anomalies are seen in the Δt^* map. Low velocities are also seen along the Appalachians with the amplitudes of the Appalachian anomalies being largest in the north and smallest in the South. These match the band of high attenuation seen along the Appalachians in our model although the attenuation anomalies follow an inverse amplitude pattern, with higher attenuation in

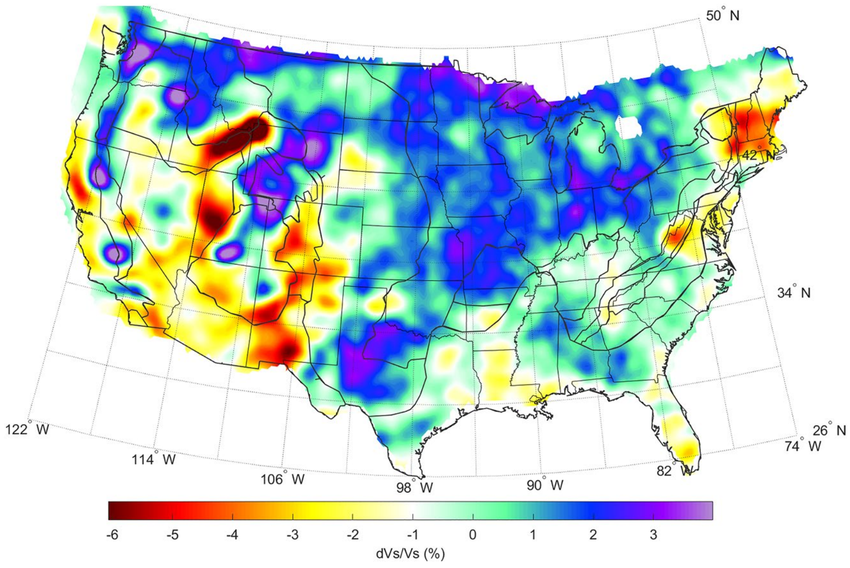

Figure 7. Shear wave velocity anomalies in the study area averaged between 80 and 250 km depth, from the model of Schmandt and Lin (2014). Thinner black lines show state boundaries, thicker black lines show tectonic province boundaries.

21699356, 2023, 12, Downloaded from https://agupubs.onlinelibrary.wiley.com/doi/10.1029/2023JB027299, Wiley Online Library on [11/12/2023]. See the Terms and Conditions (https://onlinelibrary.wiley.com/terms-and-conditions) on Wiley Online Library for rules of use; OA articles are governed by the applicable Creative Commons License

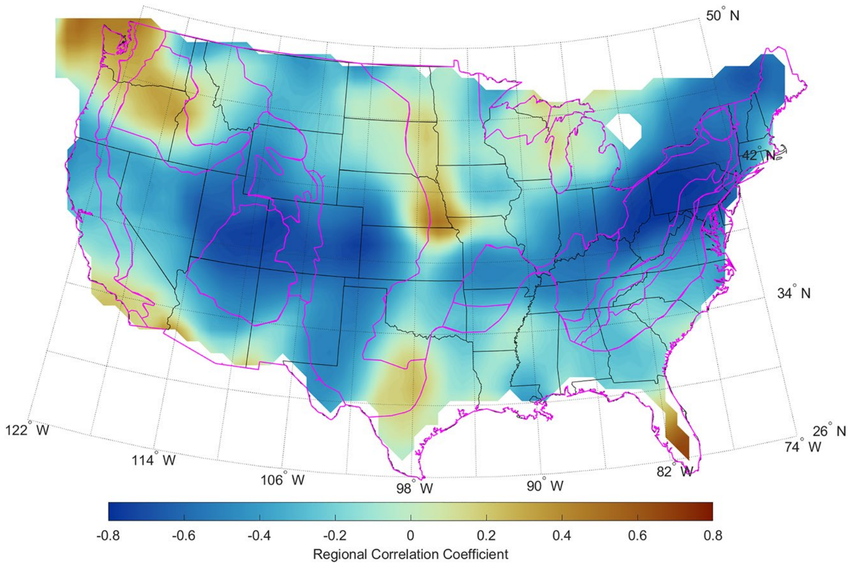

Figure 8. Local correlation between the attenuation model presented in this study (Figure 5) and the depth-averaged shear wave velocity anomaly model of Schmandt and Lin (2014) (Figure 7). At each point, the map shows the correlation values between the two anomaly maps in a 500-km radius around that point, as described in the text. Black lines show state boundaries, tectonic boundaries are shown by the magenta lines.

the southern Appalachians than in the north. South and east of the Appalachians and in the Gulf Coast region, velocity anomalies are relatively small. This is in contrast with attenuation anomalies in these regions, that vary substantially.

In summary, in broad terms, the distribution of the depth-averaged velocity anomalies and attenuation anomalies follow the expected correspondence between low velocities and high attenuation (and vice versa) with a correlation coefficient of −0.45. Although the anticorrelation is significant, the plot of Δt^* versus dV_s/V_s shows substantial scatter (Figure 6b) and the single value of the correlation coefficient obscures any spatial patterns in the co-variation of the variables. To examine these spatial patterns, we find a regional correlation coefficient at each node in our model. We calculate the correlation between Δt^* and averaged velocity anomaly in circular regions with a 500 km radius centered in each of the Δt^* model nodes. The resulting map (Figure 8) shows the highest anti-correlations in the area surrounding the CP and in the central Appalachians, with positive correlations (the opposite of what is expected) in the NW and SE extremes of the study area, as well as localized areas of positive correlation in the central and south-central of the study area.

Aside from the co-variation in velocity and attenuation anomalies, an interesting observation is that the amplitude of attenuation variations in the interior and SE of the study area seem large, with respect to the magnitude of variations in velocity, whereas some large variations in velocity correspond to only modest variations in attenuation (most notably the case of the SRP, where there is no local attenuative anomaly, but also the western U.S. more generally). To quantify this observation, we calculate the ratio of the amplitude of velocity variations to attenuation variations in a regionalized manner analogous to our calculation of regional correlation (i.e., in circular regions with a 500 km radius centered on each Δt^* model node). There are different ways to quantify the amount of variation in model parameters in each circular region. We choose to take the difference between the 90th percentile and the tenth percentile to avoid the metric being dominated by extreme values. Thus defined, the anomaly amplitudes in the velocity model are highest in the western U.S. and the NE Appalachians, while they are smallest in the north-central and southeastern U.S. (Figure S11a in Supporting Information S1). In contrast, the largest variations in Δt^* occur just west of the southern Rocky Mountains and in the SE U.S.; Δt^* variations are relatively high in the north-central U.S. and very low in the NE Appalachians (Figure S11b in Supporting Information S1).

Taking the ratio of these two maps (dividing velocity amplitudes by Δt^* amplitudes) gives a quantitative idea of where attenuation variations are large when compared to velocity variations and vice versa. To simplify the discussion, we will refer to the base-10 logarithm of the ratio between the velocity anomaly amplitudes and

21699356, 2023, 12, Downloaded from https://agupubs.onlinelibrary.wiley.com/doi/10.1029/2023JB027299, Wiley Online Library on [11/12/2023]. See the Terms and Conditions (https://onlinelibrary.wiley.com/terms-and-conditions) on Wiley Online Library for rules of use; OA articles are governed by the applicable Creative Commons License

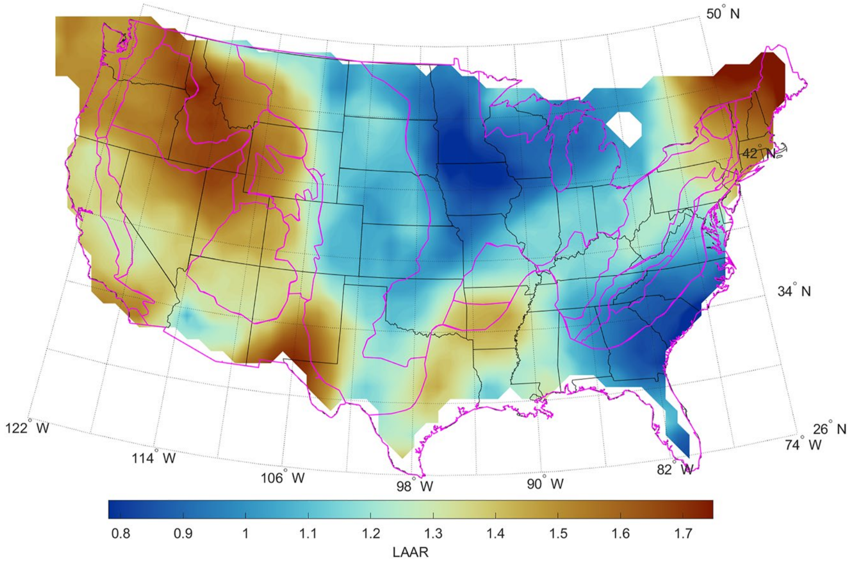

Figure 9. Base-10 logarithm of the ratio between the amplitude of attenuation anomalies (Figure S11a in Supporting Information S1) and the amplitude of shear wave velocity anomalies (Figure S11b in Supporting Information S1) calculated as described in the text. Black lines show state boundaries, tectonic boundaries are shown by the magenta lines.

the attenuation anomaly amplitudes as the Log Anomaly Amplitude Ratio (LAAR). Higher values of LAAR indicate that variations in velocity are large when compared to the variations in Δt^*; lower LAAR values indicate the opposite. The result shows that west of the RMF, lateral variations in velocity are large compared to the magnitude of attenuation variations, with LAAR values generally exceeding 1.3 and reaching ~1.6 around the SRP-Y area and the Rio Grande Rift (Figure 9). This is also the case for the northern Appalachians (LAAR of ~1.6) and less so for the central and southern Appalachians (Figure 9). The Ouachita Mountains region and eastern TX also show high ratios of velocity variability to attenuation variability (LAAR of ~1.4, Figure 9). The region between the RMF and the Appalachians has generally lower LAAR values (<1.1, Figure 9), indicating that lateral changes in attenuation are large with respect to velocity variations. The regions with the lowest LAAR are the north-central U.S. and SE of the Appalachians, where values drop to below 0.9 (Figure 9).

To provide context that helps interpret these values, we use the Very Broadband Rheology Calculator (VBR, Havlin et al., 2021) to calculate attenuation and velocity anomalies under different end-member conditions. We assume that the source of the anomalies are exclusively changes in either mantle potential temperature, grain size, or melt fraction. We note that melt-fraction and temperature variations would co-occur in nature, but we treat them independently to generate reference values for LAAR rather than to model a geologically feasible scenario. To keep this exercise simple, we assume a fixed thermal boundary layer thickness of 100 km with a conductive and adiabatic geotherm above and below that depth. We hold two of the three mantle state variables fixed each time and vary the third according to the values shown in Table 1.

We use the extended Burgers pseudoperiod method (Havlin et al., 2021; Jackson & Faul, 2010) to calculate the V_s and Q_s at 1 km depth intervals and then calculate the expected t^* for P waves as:

$$t_p^* = \sum_{z=0}^{400} \frac{1}{1.76 V_{s_z}\, 2.25 Q_{s_z}} \tag{2}$$

Assuming a constant V_p/V_s ratio of 1.76 and Q_p/Q_s ratio of 2.25 which is the expectation assuming a Poisson solid and zero bulk attenuation (e.g., Romanowicz & Mitchell, 2015). The equivalent to our LAAR is then calculated as:

$$\mathrm{LAAR} = \log_{10}\left(\frac{V_{s_{\mathrm{anom\,max}}} - V_{s_{\mathrm{anom\,min}}}}{t^*_{\mathrm{p\,max}} - t^*_{\mathrm{p\,min}}}\right) \tag{3}$$

Table 1
Values Used in Reference Log Anomaly Amplitude Ratio Value Calculations

Mantle state variable	Fixed value	Range
Potential temperature	1,350°C	1,250–1,450°C
Grain size	5 mm	0.5–20 mm
Melt fraction	0%	0%–1%

21699356, 2023, 12, Downloaded from https://agupubs.onlinelibrary.wiley.com/doi/10.1029/2023JB027299, Wiley Online Library on [11/12/2023]. See the Terms and Conditions (https://onlinelibrary.wiley.com/terms-and-conditions) on Wiley Online Library for rules of use; OA articles are governed by the applicable Creative Commons License

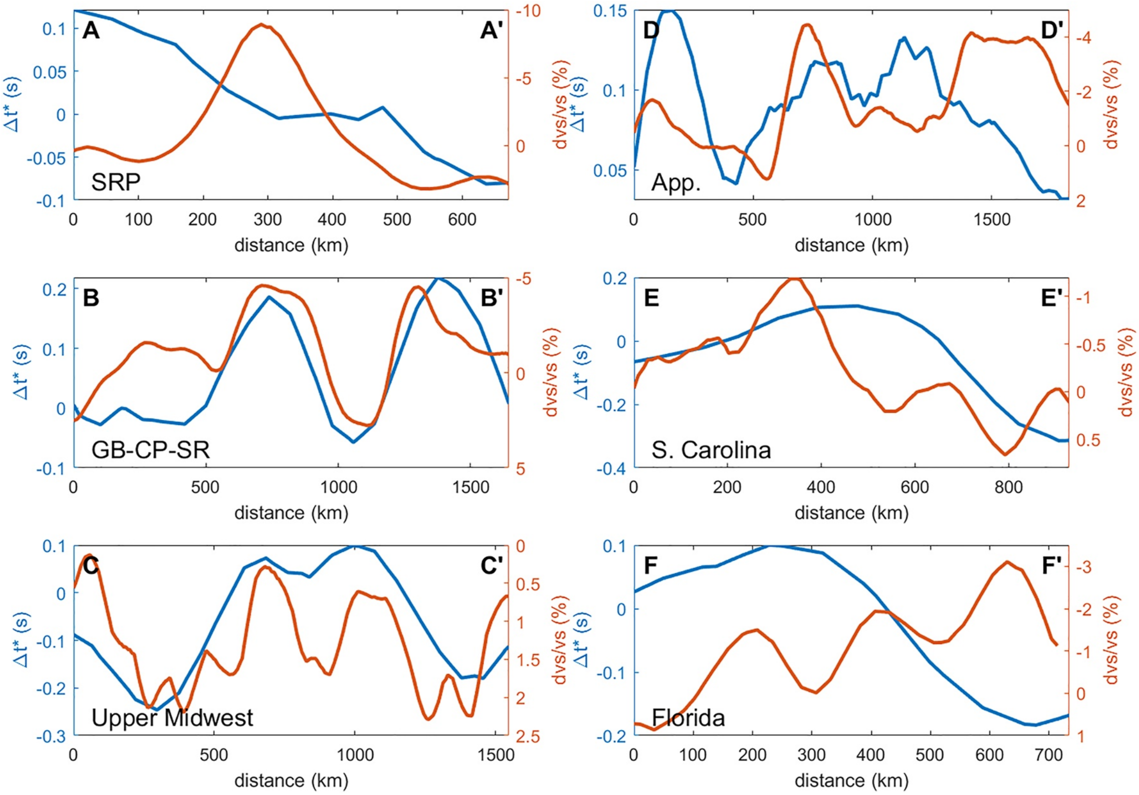

Figure 10. Comparison of Δt^* from this study and depth-averaged shear wave velocity anomalies in the model of Schmandt and Lin (2014) (Figure 7) along different profiles. For the location of the profiles, see Figure 5. Note that the axis for dV_s/V_s is inverted (i.e., values increase downward) to facilitate comparison between the two sets of observations. Note also that the scale in the *Y* axis is different for each panel. Figure S10 in Supporting Information S1 shows the same information with uniform *Y* axis scales in all panels. Abbreviations: GB, Great Basin; CP, Colorado Plateau; SR, Southern Rockies; App., Appalachians.

where $V_{s_{anom}}$ is the average shear wave velocity anomaly between 80 and 250 km, and the max and min subscripts indicate the maximum and minimum calculated values for the range of conditions. The LAAR values we obtain are compatible with those calculated from the attenuation and depth-averaged velocity maps. Varying only grain size results in a LAAR of 0.89, close to the lower end of what we observe and similar to the values seen in the upper Midwest and SE of the Appalachians. Varying the mantle potential temperature produces a LAAR of 1.23, which is slightly below what is observed in most of the western U.S. and the central and southern Appalachians. Finally, variations only in melt fraction give the highest LAAR values of 2.0, which are above the highest values observed in the study area. Using instead the constitutive model of Yamauchi and Takei (2016) yields similar LAAR values for temperature and grain size variations of 1.45 and 0.81, respectively. There are several assumptions and approximations involved in these calculations but they are valuable in two ways: (a) They show that the LAAR values that we obtain from comparing our model to that of Schmandt and Lin (2014) are broadly consistent with the range of values expected from experimental constraints on the variation of attenuation and velocity under different mantle conditions; and (b) They provide a loose reference frame for interpreting the lateral variations in LAAR that we observe. This framework suggests that temperature variations, locally with some contribution from melt fraction, dominate heterogeneity in the more tectonically active western U.S. and the Appalachians, whereas grain size variations are the more important source of lateral heterogeneity in the interior of the continent and in the accreted terranes east of the Appalachians.

4.2. Regional Cross-Sections

To continue exploring the relationship between Δt^* and dV_s/V_s, we now focus on profiles that cross important features in both models, allowing us to examine in more detail the spatial correspondence between specific attenuation and velocity anomalies.

21699356, 2023, 12, Downloaded from https://agupubs.onlinelibrary.wiley.com/doi/10.1029/2023JB027299, Wiley Online Library on [11/12/2023]. See the Terms and Conditions (https://onlinelibrary.wiley.com/terms-and-conditions) on Wiley Online Library for rules of use; OA articles are governed by the applicable Creative Commons License

21699356, 2023, 12, Downloaded from https://agupubs.onlinelibrary.wiley.com/doi/10.1029/2023JB027299, Wiley Online Library on [11/12/2023]. See the Terms and Conditions (https://onlinelibrary.wiley.com/terms-and-conditions) on Wiley Online Library for rules of use; OA articles are governed by the applicable Creative Commons License

4.2.1. The Snake River Plain—Yellowstone

Yellowstone and the eastern Snake River Plain (SRP-Y) are characterized in seismic velocity models by large-amplitude low-velocity anomalies. In the depth-averaged model of SL, dV_s/V_s anomalies exceed 8% (Figure 7; Figure 10, profile A-A'). As mentioned in Section 3, we do not find the corresponding high attenuation anomaly that one would expect. We rule out this being simply an issue with the resolution of the Δt^* model as our results suggest that the TA should provide adequate station coverage to recover this anomaly. For example, the spatial extent of the SRP-Y anomaly is comparable to that of the high-velocity anomaly at the core of the CP (Figure 5), for which we image the expected low-attenuation counterpart anomaly. Additionally, there are several other attenuation anomalies in the map that have a similar or smaller spatial extent. Therefore, the missing SRP-Y anomaly is not the result of insufficient spatial resolution.

Looking at a profile of velocity and attenuation anomalies perpendicular to the trend of the SRP (Figure 10, profile A-A'), we see that the large local minimum in velocity is superimposed on a slight gradient from higher background velocities in the SE to lower (neutral) velocity anomalies in the NW. The broad pattern of attenuation in consistent with this regional trend as it goes from lower attenuation in the SE to higher attenuation in the NW (Figure 10, profile A-A'). Instead of a large increase in attenuation over the SRP, though, we find a small local reduction in attenuation. Removing the regional trends makes this minimum in attenuation clearer (Figure S12 in Supporting Information S1).

The combination of a general agreement in long wavelength structure and strong disagreement in the short-wavelength, large-amplitude SRP anomaly gives a correlation coefficient between dV_s/V_s and Δt^* along this profile of only −0.14. The LAAR calculated along this profile is the highest in the study area, reaching a value of 1.77, which approaches our reference value for the melt-only case.

4.2.2. The Great Basin, Colorado Plateau, and Southern Rockies

Depth-averaged velocity anomalies and attenuation anomalies are strongly anticorrelated along this profile (correlation coefficient of −0.77). The core of the CP shows high velocities and low attenuation and is flanked by low velocity and high attenuation anomalies. To the west, in the Great Basin, velocities increase and attenuation decreases (Figure 10, profile B-B'). The spatial correspondence between the changes in velocity and the corresponding change in attenuation is remarkable as evidenced by the very high anticorrelation coefficient. The LAAR value for this profile is 1.48 which is above the values expected for exclusively thermal variations from our VBR calculations.

4.2.3. The Upper Midwest

Velocity anomalies in the north-central U.S., a geographic region often referred to as "the upper Midwest," are generally positive (i.e., higher than average) as expected for the cratonic core of the continent. In contrast, our attenuation model shows relatively high attenuation in this area, which is puzzling. However, if we consider a profile going roughly E-W across this region and compare the values of Δt^* and dV_s/V_s we find that the relative changes in attenuation and shear wave velocity mimic each other (Figure 10, profile C-C') showing a correlation coefficient of −0.49. Qualitatively, the variations in Δt^* look smoother than those in velocity and it is reasonable to expect that a higher resolution Δt^* model would produce an even stronger anticorrelation with the velocity model. The LAAR calculated along this profile is 0.75, which is among the lowest values anywhere in the model and a close fit to the case that considers only grain-size variations.

4.2.4. The Appalachians

The Appalachian Mountains are characterized by high attenuation and low velocity anomalies. There are two distinct low-velocity anomalies that have received attention in the literature recently, the Northern Appalachian Anomaly (Dong & Menke, 2017; Goldhagen et al., 2022; Levin et al., 2018; Menke et al., 2016, 2018) and the Central Appalachian Anomaly (e.g., J. S. Byrnes et al., 2019; Evans et al., 2019; Long et al., 2021). The origin of these anomalies is still debated, including whether they have similar or perhaps connected origins, but thinned lithosphere and mantle upwelling is implicated in both cases (e.g., J. S. Byrnes et al., 2019; Goldhagen et al., 2022; Long et al., 2021; Menke et al., 2018). Consequently, a positive attenuation anomaly is expected. A smaller anomaly is seen in the depth-averaged velocity model of Schmandt and Lin (2014) in the southern Appalachians (Figure 7) that Carrero Mustelier and Menke (2021) refer to as the Southern Appalachian Anomaly.

Similarly, in our model there are three local maxima in attenuation along the Appalachian trend (Figure 10, profile D-D') although their characteristics differ from what is seen in velocity models. The southernmost attenuation

21699356, 2023, 12, Downloaded from https://agupubs.onlinelibrary.wiley.com/doi/10.1029/2023JB027299, Wiley Online Library on [11/12/2023]. See the Terms and Conditions (https://onlinelibrary.wiley.com/terms-and-conditions) on Wiley Online Library for rules of use; OA articles are governed by the applicable Creative Commons License

anomaly corresponds spatially to the southern velocity anomaly but while the velocity anomaly is small relative to the other Appalachian anomalies, the attenuation is highest along this section of the mountain range. In the central Appalachians the velocity and attenuation anomalies broadly correspond spatially although the attenuation anomaly is shifted to the SW by ~75 km. The northern anomalies in the two models do not correspond to each other. The northernmost peak in attenuation in the Appalachians occurs between the central and northern Appalachian velocity anomalies. We do not find an attenuation anomaly that corresponds to the large amplitude velocity anomaly in the northern Appalachians, but rather attenuation in our model decreases there. We note that in the Cafferky and Schmandt (2015) attenuation model there is positive anomaly that largely corresponds to the NAA, while in the work of Dong and Menke (2017) the attenuation high occurs to the west of the NAA. The partial correspondence between velocity and attenuation anomalies along this profile produces a modestly positive correlation coefficient of 0.14. If we exclude the part of the profile north of the Central Appalachian Anomaly, we obtain a value of −0.44 reflecting the better spatial correspondence between attenuation and velocity anomalies in the southern part of the profile; mismatches in anomaly amplitude notwithstanding. The LAAR for this profile is 1.67, which is substantially higher than the reference values calculated for temperature variations exclusively and approaches the melt-only case.

4.2.5. Low Attenuation Regions in the Southeastern U.S.

The prominent low attenuation regions in the central Gulf coast, eastern South Carolina and southern Florida, do not correlate well with velocity. These features appear to be statistically robust (Figures S3 and S7 in Supporting Information S1) though they lie near the edge of station coverage. Each anomaly occurs in a tile processed independently by two analysts and is produced by the inversion in each case (Figure 4), with amplitudes that differ at a level near the error. The western boundary of the South Carolina anomaly aligns with the edge of the Appalachian piedmont, showing consistency between anomaly geometry and geological boundaries. Although the velocity anomalies have modest amplitudes in this region, the overall pattern is consistent with attenuation, as there is a local maximum in velocity near the coast (Figure 10, profile E-E’). This results in a correlation coefficient along this profile of −0.58. In contrast with velocity anomalies, variations in attenuation are very large in this part of the model. This results in an LAAR value of 0.55, the lowest anywhere in the model and substantially lower than the reference values calculated for variations in grain size exclusively. In Florida, both attenuation and velocity tend to decrease toward the south (Figure 10, profile F-F’) resulting in a positive correlation coefficient of 0.70. This is the part of the model where the relationship between attenuation and velocity anomalies seems the most perplexing.

4.3. Caveats

There are several simplifications that we have made in our analysis; here we consider how sensitive our conclusions are to those simplifications. First, we consider the issue of anisotropy. Azimuthal velocity anisotropy is well-documented across the study area from shear wave splitting (K. H. Liu et al., 2014; Long et al., 2016), surface wave (Lin et al., 2011; Lin & Schmandt, 2014), and receiver function (Schulte-Pelkum & Mahan, 2014) analyses. Given the steep incidence angles in the depth interval of interest of the teleseismic *P*-waves we analyze, we argue that any effects of azimuthal anisotropy in velocity or in *Q* are negligible. One potential way in which velocity anisotropy could affect our results is in the determination of velocity anomaly amplitudes that go into the LAAR calculation. Studies have shown that teleseismic tomography studies that assume isotropic propagation (such as the one we use here, Schmandt & Lin, 2014) may overestimate the amplitude of low-velocity anomalies where strong anisotropy with near-horizontal fast axes is also present (e.g., Bezada et al., 2016; VanderBeek & Faccenda, 2021; VanderBeek et al., 2023). Since in this study we are focusing on the continental scale patterns, we leave the consideration of how this effect might locally affect the LAAR to future investigations.

More important is the simplifying assumption of singular values for V_p/V_s and Q_p/Q_s ratios. These values are needed in order to compare our *P*-wave attenuation results to shear wave velocity models and to VBR calculations that output V_s and Q_s, and evidence suggests their true values will be locally different from the ones we have chosen. Whereas we have used a single V_p/V_s ratio of 1.76, tomography models show variations in V_p/V_s in the upper mantle of our study area of up to ±3% (Golos et al., 2020). Changing the value used in the forward LAAR calculation by those amounts, and using the constitutive equations of JF10 results in thermal LAAR values of 1.24 and 1.21 (in comparison to our value of 1.23) which as a much smaller change than the range of our LAAR observations. Also important is the assumption of a single Q_p/Q_s. The value we have used ($Q_p/Q_s = 2.25$)

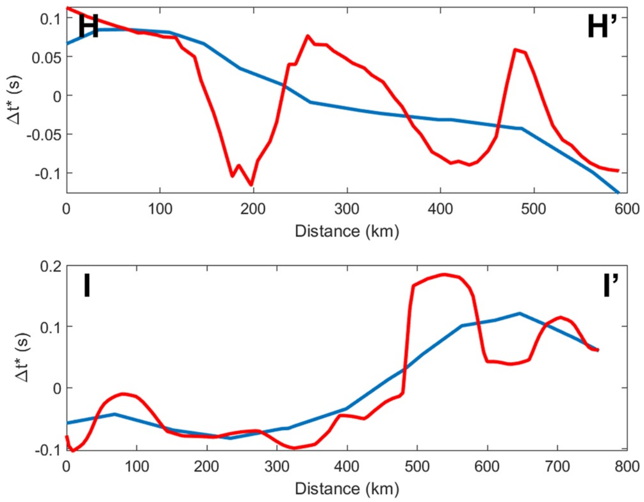

Figure 11. Δ*t** from this study (blue lines) and from higher resolution studies (red lines) across profiles in Wyoming (H-H’, Zhu et al., 2021) and the Central Appalachian Anomaly (I-I’, J. S. Byrnes et al., 2019). In each case, the mean value across the profile has been removed to facilitate the comparison. For the location of the profiles, see Figure 5.

is a common approximation that neglects bulk attenuation (Romanowicz & Mitchell, 2015), however studies that have estimated Q_p/Q_s from observations have occasionally reached values as low as <1.5 (Wei & Wiens, 2020). Using a very low Q_p/Q_s value of 1.5 in the calculations substantially reduces the thermal LAAR (using the constitutive equations of Jackson & Faul, 2010) to a value of 1.05; yet this is still above the <0.9 observed in some regions of our model. Such extreme values of Q_p/Q_s are only likely to occur in regions of intense melting, and much smaller variations are expected across most of the study area. It is clear, then, that although there is a range of possible theoretical thermal LAAR, this range is exceeded by our observations. We therefore reject the hypothesis that our observed lateral variations in LAAR result only from neglecting lateral variations in V_p/V_s or Q_p/Q_s.

5. Relationship to Local Attenuation Studies

The method we employ here for measuring Δ*t** has been used in other regional studies in the continental U.S. (J. S. Byrnes & Bezada, 2020; J. S. Byrnes et al., 2019; Zhu et al., 2021). These studies include data from denser temporary seismic array deployments with station spacing below the nominal 70 km value of the USArray TA. In particular, the Zhu et al. (2021) model for northern Wyoming and surrounding regions uses data from the BASE (e.g., Worthington et al., 2016) and CIELO (Ford et al., 2021) deployments, the latter having average station spacing of 19 km, which locally decreased to 4 km. The study of J. S. Byrnes et al. (2019) across the Central Appalachians utilizes data from the MAGIC array (Long et al., 2020) with a station spacing between 30 and 15 km. These denser deployments allow for higher resolution imaging, and the studies in question used a trans-dimensional Bayesian approach to building the Δ*t** map that is designed for better recovering sharp gradients (J. S. Byrnes et al., 2019). In this section we assess the limits of the resolution of our model by comparing it to the higher-resolution models across two profiles.

In Wyoming, we find that our continental-scale model recovers only the broad trend of decreasing attenuation from west to east, but not the small scale (∼100 km width or narrower) features that can be seen superimposed on this trend in the regional model (Figure 11, profile H-H’). Similarly, on the profile across the Central Appalachians, we see that our continental-scale model recovers a substantially smoother version of the regional model. Instead of the sharp gradients on either side of the high-attenuation anomaly, we see a broad and gently sloping peak (Figure 11, profile I-I’). Additionally, the local maximum in attenuation is shifted to the east by ∼100 km with respect to the regional model. We conclude that even though our model reveals substantial short-wavelength lateral variations in attenuation structure, it is still a smooth representation of the true structure. As a corollary, continental lithospheric structure likely possesses even more lateral heterogeneity than what is suggested by our attenuation model.

6. Relationship With Lithospheric Thickness and Thermotectonic Ages

Given the big differences in *Q* between lithosphere and asthenosphere (e.g., Romanowicz & Mitchell, 2015 and references therein), we expect the depth of the Lithosphere-Asthenosphere Boundary (LAB) and the observed attenuation to be substantially anticorrelated (as in Deng et al., 2021). We find a correlation coefficient of −0.51 between our Δ*t** map and the LAB depths in the LITHO1.0 model (Figure S13a in Supporting Information S1, Pasyanos et al., 2014). This is slightly larger than the anticorrelation values between Δ*t** and depth-averaged velocity from the model of Schmandt and Lin (2014). Meanwhile, the anticorrelation between the LAAR values and LAB depths is substantially larger, reaching a value of −0.73. This shows that in regions with thicker lithosphere, LAAR values are consistently smaller; meaning the lateral variations in attenuation are large compared to the size of variations in velocity. In regions with thinner lithosphere, the opposite is true.

Separating the study area into regions with thick (LAB deeper than 200 km), thin (LAB shallower than 100 km) and intermediate lithosphere we see differences in the LAAR values for the thick and thin lithosphere regions. Although there is some overlap in the range of values for the thin and thick lithosphere sets, the interquartile

21699356, 2023, 12, Downloaded from https://agupubs.onlinelibrary.wiley.com/doi/10.1029/2023JB027299, Wiley Online Library on [11/12/2023]. See the Terms and Conditions (https://onlinelibrary.wiley.com/terms-and-conditions) on Wiley Online Library for rules of use; OA articles are governed by the applicable Creative Commons License

21699356, 2023, 12, Downloaded from https://agupubs.onlinelibrary.wiley.com/doi/10.1029/2023JB027299, Wiley Online Library on [11/12/2023]. See the Terms and Conditions (https://onlinelibrary.wiley.com/terms-and-conditions) on Wiley Online Library for rules of use; OA articles are governed by the applicable Creative Commons License

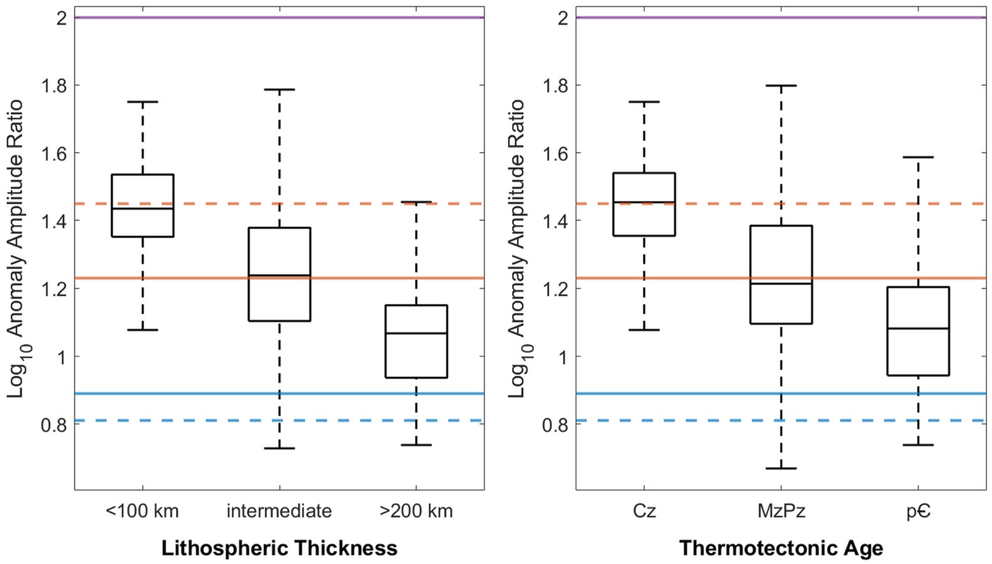

Figure 12. Box plots of Log Anomaly Amplitude Ratio (LAAR) values for parts of the study area with different lithospheric thicknesses (from the LITHO 1.0 model, Pasyanos et al., 2014) and with different thermotectonic ages (from the age model of R. C. Porter et al., 2019) as labeled on the figure. In each case the boxes represent the interquartile range, with the horizontal line within the box indicating the median value. Whiskers extend to the range of all the values in each group excluding outliers, defined as values more than 2.7 standard deviations from the mean. Horizontal lines show reference LAAR values calculated with the VBR (Havlin et al., 2021) as described in Section 4.1. Blue lines are reference values for exclusively grain size variations, orange lines are reference values for exclusively thermal variations and the purple line is the reference value for exclusively melt fraction variations. Reference LAAR values indicated with solid lines were calculated using the constitutive equations of Jackson and Faul (2010), and those indicated with dashed lines were calculated using the constitutive equations of Yamauchi and Takei (2016). Age abbreviations: Cz, Cenozoic; MzPz, Mesozoic and Paleozoic; p€, Precambrian.

regions in each case do not overlap (Figure 12). For the thick lithosphere set, the interquartile region lies entirely between the LAAR reference values for exclusively grain size variations and exclusively temperature variations (Figure 12). In the case of the thin lithosphere set, the LAAR interquartile region lies between the LAAR reference values for exclusively temperature variations and the reference value for exclusively variations in melt fraction. Regions with lithospheric thicknesses between the two thresholds have LAAR values spanning the whole range observations. We note that the choice of a 100 km Thermal Boundary Layer thickness when calculating the reference LAAR values does not exert any control on these results. Changing the reference TBL depth in those calculations to 70 km, 150, and 200 km gives reference purely thermal LAAR values of 1.18, 1.25, and 1.29 respectively. For the purpose of this discussion, these are all functionally equivalent to the 1.23 reference value we are using. Furthermore, using a thicker TBL to calculate the reference thermal LAAR gives a slightly larger value, whereas the LAAR values we observe in thicker-lithosphere regions are substantially lower than our reference thermal value.

We can also compare the map of LAAR to the thermotectonic age model of R. C. Porter et al. (2019) (Figure S13c in Supporting Information S1). This model was built from the igneous rock dates in the EarthChem database and provides a good estimate for the ages of the last episode of tectonic activity across the study area. We find a correlation coefficient between age and Δt^* of −0.45 whereas the correlation coefficient between LAAR and age is higher, reaching −0.55. The inverse correlation means that areas with older thermotectonic ages have smaller LAAR values and vice versa. If we separate the study area by the recency of tectonic activity, we find a very similar distribution of LAAR with age as we do with lithospheric thickness (Figure 12). Regions with tectonic activity in the Cenozoic have LAAR values whose interquartile region lies between the purely thermal and purely melt-driven reference values. Regions where the most recent tectonic activity occurred in the Precambrian have LAAR values with interquartile regions below the thermal reference value and the grain-size reference value. For those regions with most recent tectonic activity in the Mesozoic or Paleozoic, LAAR values span the whole range of observations.

21699356, 2023, 12, Downloaded from https://agupubs.onlinelibrary.wiley.com/doi/10.1029/2023JB027299, Wiley Online Library on [11/12/2023]. See the Terms and Conditions (https://onlinelibrary.wiley.com/terms-and-conditions) on Wiley Online Library for rules of use; OA articles are governed by the applicable Creative Commons License

7. Discussion and Conclusions

We have shown that teleseismic attenuation measurements in the study area are broadly repeatable and generally anticorrelated with velocity anomalies as expected from theory and experimental constraints. Importantly, the variations in attenuation in tectonically quiescent areas are substantial, even where velocity anomalies are modest. We have quantified this observation using the LAAR parameter and shown that there are spatial variations in this quantity that are consistent with known mantle structure and tectonic history. Regions with thicker and thinner lithosphere show lower and higher LAAR values, respectively. Spatial patterns in velocity and attenuation anomalies are typically consistent, regardless of the ratio between velocity and attenuation anomaly amplitudes. For example, the profile across the CP shows very good consistency between velocity and attenuation (see Figure 10, profile B-B' and discussion in Section 4.2.2) and high values of LAAR, whereas in the upper Midwest, very low values of LAAR coexist with a good correspondence between local maxima in attenuation and minima in velocity (see Figure 10, profile C-C' and discussion in Section 4.2.3). The comparison of our model to higher resolution regional attenuation models in Section 4.3 suggests that, in the Upper Midwest, a higher resolution attenuation model may yield sharper peaks in attenuation that more closely mimic the lateral variations in velocity. This spatial correspondence of anomalies implies that the variations in attenuation that we measure are reflecting the same variations in mantle structure that are imaged in velocity tomography models but with greater sensitivity in tectonically quiescent regions.

We use the LAAR analysis to shed light on the reasons behind these variations in sensitivity and the results suggest that while temperature and melt fraction dominate heterogeneity in regions with thinner lithosphere and more recent tectonic activity (with higher LAAR values), grain size variations are the most important form of mantle heterogeneity in thick-lithosphere, tectonically quiescent regions (where we see low LAAR values). Using the set of conditions listed in Table 1, we obtained a maximum variation in t^* of due exclusively to grain size variations of 0.34 s. This is very similar to the range in Δt^* obtained along the Upper Midwest profile (Figure 10c) of 0.35 s. Higher lithospheric thicknesses would lower the size of maximum t^* variation attributable to grain size, and decreasing the lower end of the grain size range would increase this value. We do not suggest that grain size is the only source of variations in Δt^* in the continental interior, but these calculations show that it is plausible that they can contribute a significant fraction thereof. We should also consider what could be the source of lateral variations in grain size, since grain size in the mantle is a product of the equilibrium between grain growth and dynamic grain size reduction (Austin & Evans, 2007). We note that there are conditions that can vary laterally and that affect these processes. For example, the presence of pores or pinning phases can inhibit grain growth (e.g., Karato, 1989; Tasaka & Hiraga, 2013) and moderate water concentrations can enhance it (e.g., Karato, 1989). We conclude that teleseismic attenuation may be an indicator of lateral changes in grain size in continental interiors, which would in turn provide additional insights into grain size evolution processes, and these research avenues should be explored.

We note that our LAAR calculations utilize the range of anomaly values present in the seismic models, which are modulated by the regularization parameters used. At the same time, in both the attenuation and velocity model, regularization is applied evenly across the study area, so lateral variations in anomaly amplitudes are robust. Further, being that we are taking the base-10 logarithm of the anomaly amplitude ratios, our metric is only weakly sensitive to the variations in amplitude that can be expected by implementing different regularization parameters.

Tectonic activity in the western U.S. (where LAAR is highest) is generally much more recent than in the Appalachians (the other part of the model with high LAAR values), yet magmatic activity in parts of the Appalachians has been documented as recently as the Eocene (e.g., Mazza et al., 2017). High-amplitude velocity anomalies have been consistently observed in the northern and central Appalachians and the joint interpretation of multiple geophysical constraints favors the presence of melt in at least the central Appalachians (e.g., Mittal et al., 2023).

The most notable instance of melt fraction seemingly affecting velocity more than attenuation is the Yellowstone-Snake River Plain region, where abundant recent magmatism (e.g., Smith & Siegel, 2000; Smith et al., 2009) and extremely low shear wave velocities in the mantle (e.g., Schmandt & Lin, 2014; Shen & Ritzwoller, 2016; Stanciu & Humphreys, 2020) imply high melt fractions, yet attenuation is not elevated and a synthetic test suggests this is unlikely to be solely a resolution issue. Given the strength of the anomaly in velocity, an alternative explanation for this observation is that focusing effects obscure a positive anomaly in attenuation. We note there is no attenuation anomaly in the SRP-Y in models of surface wave attenuation (Bao et al., 2016), and focusing effects may be a plausible explanation given the longer periods involved. As mentioned in Section 3.2.1, 1 Hz *P* waves should not feature focusing artifacts at these length scales (J. S. Byrnes et al., 2019) but given the station coverage and the strength of the anomaly, we concede that focusing effects should be considered further. We also note that the small local minimum in attenuation that we observe is consistent with the low attenuation imaged by Adams and Humphreys (2010) in the Yellowstone region. Adams and Humphreys (2010) proposed that the weak attenuation was due to dehydration of the upper mantle due to melting, with melt not enhancing attenuation (Hammond & Humphreys, 2000). Previous studies have shown that melt fraction must have an effect on attenuation (e.g., Abers et al., 2014). What our study suggests is that this effect is small compared to the effect that melt fraction has on velocity. Further complications arise because the melt fraction value alone does not capture all the relevant complexity. The viscosity of the melt and the geometry of how it is distributed in the intergranular space will have an impact on how it may or may not produce attenuation in the seismic frequency band (Hammond & Humphreys, 2000). Attempting to characterize the distribution and characteristics of partial melt in the mantle is beyond the scope of this study. We aim only to show that there is a broad general pattern that seems to associate the ratio between velocity and attenuation anomalies to the likelihood of the presence of melt.

Our study demonstrates the potential for gaining additional insights about upper mantle structure by studying lateral variations in teleseismic attenuation. Attenuation may be especially useful in continental interiors and other tectonically quiescent regions as anomaly amplitudes are large, and features that may be inconspicuous in velocity models become prominent in attenuation models.

Data Availability Statement

All the data used in this study is available through the IRIS Data Management Center. The relevant networks are USArray Transportable Array (IRIS Transportable Array, 2003) and the Southern California Seismic Network (California Institute of Technology and United States Geological Survey Pasadena, 1926). The waveforms used for analysis, best-fit synthetic waveforms, Δt^* measurements and QC results for each case are archived in the Data Repository for the University of Minnesota (DRUM) and can be accessed at Bezada et al. (2023) https://doi.org/10.13020/qy6j-h516.

Acknowledgments

We thank one anonymous reviewer and an associate editor for constructive reviews on an earlier version of this manuscript that inspired many improvements. We also thank associate editor Brandon Schmandt and reviewers Geoff Abers and Vadim Levin for thorough and insightful reviews. Additionally, we thank Brandon Schmandt for sharing the Cafferky and Schmandt (2015) model in digital form, Ryan Porter for providing a digital copy of the Thermotectonic age model of R. C. Porter et al. (2019), and Lars Hansen for his insights during conversations about this manuscript. This study was made possible by the access to data and metadata provided by the IRIS Data Management Center. IRIS Data Services are funded through the Seismological Facilities for the Advancement of Geoscience (SAGE) Award of the National Science Foundation under Cooperative Support Agreement EAR-1851048. The Shen and Ritzwoller (2016) and Schmandt and Lin (2014) were retrieved from the IRIS Earth Model Collaboration (https://doi.org/10.17611/DP/EMC.1). This work was partly funded by NSF Grant EAR-1944998 to Bezada.

References

Abers, G. A., Fischer, K. M., Hirth, G., Wiens, D. A., Plank, T., Holtzman, B. K., et al. (2014). Reconciling mantle attenuation-temperature relationships from seismology, petrology, and laboratory measurements. *Geochemistry, Geophysics, Geosystems*, *15*(9), 3521–3542. https://doi.org/10.1002/2014GC005444

Adams, D. C., & Humphreys, E. D. (2010). New constraints on the properties of the Yellowstone mantle plume from P and S wave attenuation tomography. *Journal of Geophysical Research*, *115*(B12), B12310. https://doi.org/10.1029/2009JB006864

Austin, N. J., & Evans, B. (2007). Paleowattmeters: A scaling relation for dynamically recrystallized grain size. *Geology*, *35*(4), 343–346. https://doi.org/10.1130/G23244A.1

Azimi, S. A., Kalinin, A. V., Kalinin, V. V., & Pivovarov, B. L. (1968). Impulse and transient characteristics of media with linear and quadratic absorption laws. *Izvestiya Physics of the Solid Earth*, *2*, 88–93.

Bao, X., Dalton, C. A., Jin, G., Gaherty, J. B., & Shen, Y. (2016). Imaging Rayleigh wave attenuation with USArray. *Geophysical Journal International*, *206*(1), 241–259. https://doi.org/10.1093/gji/ggw151

Becker, T. W. (2012). On recent seismic tomography for the western United States. *Geochemistry, Geophysics, Geosystems*, *13*(1), Q01W10. https://doi.org/10.1029/2011GC003977

Bezada, M. J. (2017). Insights into the lithospheric architecture of Iberia and Morocco from teleseismic body-wave attenuation. *Earth and Planetary Science Letters*, *478*, 14–26. https://doi.org/10.1016/j.epsl.2017.08.029

Bezada, M. J., Byrnes, J., & Eilon, Z. (2019). On the robustness of attenuation measurements on teleseismic P waves: Insights from micro-array analysis of the 2017 North Korean nuclear test. *Geophysical Journal International*, *218*(1), 573–585. https://doi.org/10.1093/gji/ggz169

Bezada, M. J., Byrnes, J., Zhu, Z., & Lee, H. (2023). *Waveforms and teleseismic attenuation measurements across the conterminous United States using EarthScope Transportable Array data*. Data Repository for the University of Minnesota. https://doi.org/10.13020/qy6j-h516

Bezada, M. J., Faccenda, M., & Toomey, D. R. (2016). Representing anisotropic subduction zones with isotropic velocity models: A characterization of the problem and some steps on a possible path forward. *Geochemistry, Geophysics, Geosystems*, *17*(8), 3164–3189. https://doi.org/10.1002/2016GC006507

Bezada, M. J., & Smale, J. (2019). Lateral variations in lithospheric mantle structure control the location of intracontinental seismicity in Australia. *Geophysical Research Letters*, *46*(22), 12862–12869. https://doi.org/10.1029/2019GL084848

Bodmer, M., Toomey, D. R., Hooft, E. E. E., & Schmandt, B. (2018). Buoyant asthenosphere beneath cascadia influences megathrust segmentation. *Geophysical Research Letters*, *45*(14), 6954–6962. https://doi.org/10.1029/2018GL078700

Buehler, J. S., & Shearer, P. M. (2017). Uppermost mantle seismic velocity structure beneath USArray. *Journal of Geophysical Research: Solid Earth*, *122*(1), 436–448. https://doi.org/10.1002/2016JB013265

Byrnes, J., Gaherty, J., & Hopper, E. (2023). Seismic architecture of the lithosphere-asthenosphere system in the western United States from a joint inversion of body- and surface-wave observations: Distribution of partial melt in the upper mantle. *Seismica*, *2*, 29. https://doi.org/10.26443/seismica.v2i2.272

21699356, 2023, 12, Downloaded from https://agupubs.onlinelibrary.wiley.com/doi/10.1029/2023JB027299, Wiley Online Library on [11/12/2023]. See the Terms and Conditions (https://onlinelibrary.wiley.com/terms-and-conditions) on Wiley Online Library for rules of use; OA articles are governed by the applicable Creative Commons License

Byrnes, J. S., & Bezada, M. (2020). Dynamic upwelling beneath the salton trough imaged with teleseismic attenuation tomography. *Journal of Geophysical Research: Solid Earth*, *125*(11), e2020JB020347. https://doi.org/10.1029/2020JB020347

Byrnes, J. S., Bezada, M., Long, M. D., & Benoit, M. H. (2019). Thin lithosphere beneath the central Appalachian Mountains: Constraints from seismic attenuation beneath the MAGIC array. *Earth and Planetary Science Letters*, *519*, 297–307. https://doi.org/10.1016/j.epsl.2019.04.045

Cafferky, S., & Schmandt, B. (2015). Teleseismic P wave spectra from USArray and implications for upper mantle attenuation and scattering. *Geochemistry, Geophysics, Geosystems*, *16*(10), 3343–3361. https://doi.org/10.1002/2015GC005993

California Institute of Technology and United States Geological Survey Pasadena. (1926). Southern California seismic Network [Dataset]. International Federation of Digital Seismograph Networks. https://doi.org/10.7914/SN/CI

Carrero Mustelier, E., & Menke, W. (2021). Seismic anomalies in the southeastern North American asthenosphere as characterized with body wave travel times from high-quality teleseisms. *Tectonophysics*, *809*, 228853. https://doi.org/10.1016/j.tecto.2021.228853

Chantel, J., Manthilake, G., Andrault, D., Novella, D., Yu, T., & Wang, Y. (2016). Experimental evidence supports mantle partial melting in the asthenosphere. *Science Advances*, *2*(5), e1600246. https://doi.org/10.1126/sciadv.1600246

Cline Ii, C. J., Faul, U. H., David, E. C., Berry, A. J., & Jackson, I. (2018). Redox-influenced seismic properties of upper-mantle olivine. *Nature*, *555*(7696), 355–358. https://doi.org/10.1038/nature25764

Deng, Y., Byrnes, J. S., & Bezada, M. (2021). New insights into the heterogeneity of the lithosphere-asthenosphere system beneath South China from teleseismic body-wave attenuation. *Geophysical Research Letters*, *48*(6), e2020GL091654. https://doi.org/10.1029/2020GL091654

Dong, M. T., & Menke, W. H. (2017). Seismic high attenuation region observed beneath southern New England from teleseismic body wave spectra: Evidence for high asthenospheric temperature without melt. *Geophysical Research Letters*, *44*(21), 10958–10969. https://doi.org/10.1002/2017GL074953

Eilon, Z. C., & Abers, G. A. (2017). High seismic attenuation at a mid-ocean ridge reveals the distribution of deep melt. *Science Advances*, *3*(5), e1602829. https://doi.org/10.1126/sciadv.1602829

Evans, R. L., Benoit, M. H., Long, M. D., Elsenbeck, J., Ford, H. A., Zhu, J., & Garcia, X. (2019). Thin lithosphere beneath the central Appalachian Mountains: A combined seismic and magnetotelluric study. *Earth and Planetary Science Letters*, *519*, 308–316. https://doi.org/10.1016/j.epsl.2019.04.046

Faul, U. H., Fitz Gerald, J. D., & Jackson, I. (2004). Shear wave attenuation and dispersion in melt-bearing olivine polycrystals: 2. Microstructural interpretation and seismological implications. *Journal of Geophysical Research*, *109*(B6), B06201. https://doi.org/10.1029/2003JB002407

Faul, U. H., & Jackson, I. (2005). The seismological signature of temperature and grain size variations in the upper mantle. *Earth and Planetary Science Letters*, *234*(1), 119–134. https://doi.org/10.1016/j.epsl.2005.02.008

Ford, H. A., Bezada, M. J., Byrnes, J. S., Birkey, A., & Zhu, Z. (2021). The CIELO seismic experiment. *Seismological Research Letters*, *93*(2A), 1063–1074. https://doi.org/10.1785/0220210237

Goldhagen, G. B., Ford, H. A., & Long, M. D. (2022). Evidence for a lithospheric step and pervasive lithospheric thinning beneath southern New England, northeastern USA. *Geology*, *50*(9), 1078–1082. https://doi.org/10.1130/G50133.1

Golos, E. M., Fang, H., & van der Hilst, R. D. (2020). Variations in seismic wave speed and VP/VS ratio in the North American lithosphere. *Journal of Geophysical Research: Solid Earth*, *125*(12), e2020JB020574. https://doi.org/10.1029/2020JB020574

Hammond, W. C., & Humphreys, E. D. (2000). Upper mantle seismic wave velocity: Effects of realistic partial melt geometries. *Journal of Geophysical Research: Solid Earth*, *105*(B5), 10975–10986. https://doi.org/10.1029/2000JB900041

Havlin, C., Holtzman, B. K., & Hopper, E. (2021). Inference of thermodynamic state in the asthenosphere from anelastic properties, with applications to North American upper mantle. *Physics of the Earth and Planetary Interiors*, *314*, 106639. https://doi.org/10.1016/j.pepi.2020.106639

Hawley, W. B., Allen, R. M., & Richards, M. A. (2016). Tomography reveals buoyant asthenosphere accumulating beneath the Juan de Fuca plate. *Science*, *353*(6306), 1406–1408. https://doi.org/10.1126/science.aad8104

Hopper, E., & Fischer, K. M. (2018). The changing face of the lithosphere-asthenosphere boundary: Imaging continental scale patterns in upper mantle structure across the contiguous U.S. With sp converted waves. *Geochemistry, Geophysics, Geosystems*, *19*(8), 2593–2614. https://doi.org/10.1029/2018GC007476

IRIS Transportable Array. (2003). USArray transportable array [Dataset]. International Federation of Digital Seismograph Networks. https://doi.org/10.7914/SN/TA

Jackson, I., & Faul, U. H. (2010). Grainsize-sensitive viscoelastic relaxation in olivine: Towards a robust laboratory-based model for seismological application. *Physics of the Earth and Planetary Interiors*, *183*(1–2), 151–163. https://doi.org/10.1016/j.pepi.2010.09.005

Karato, S. (1989). Grain growth kinetics in olivine aggregates. *Tectonophysics*, *168*(4), 255–273. https://doi.org/10.1016/0040-1951(89)90221-7

Karayazi, O. (2022). Seismic attenuation and active tectonics in Alaska (MS thesis). Retrieved from https://conservancy.umn.edu/handle/11299/243042

Lawrence, J. F., Shearer, P. M., & Masters, G. (2006). Mapping attenuation beneath North America using waveform cross-correlation and cluster analysis. *Geophysical Research Letters*, *33*(7), L07315. https://doi.org/10.1029/2006gl025813

Levin, V., Long, M. D., Skryzalin, P., Li, Y., & López, I. (2018). Seismic evidence for a recently formed mantle upwelling beneath New England. *Geology*, *46*(1), 87–90. https://doi.org/10.1130/G39641.1

Liang, X., Zhao, D., Hua, Y., & Xu, Y.-G. (2022). Mantle tomography of central-eastern USA: Influence of inversion volume size. *Journal of Geophysical Research: Solid Earth*, *127*(12), e2022JB024782. https://doi.org/10.1029/2022JB024782

Lin, F. C., Ritzwoller, M., Yang, Y., Moschetti, M., & Fouch, M. (2011). Complex and variable crustal and uppermost mantle seismic anisotropy in the western United States. *Nature Geoscience*, *4*(1), 55–61. https://doi.org/10.1038/ngeo1036

Lin, F.-C., & Schmandt, B. (2014). Upper crustal azimuthal anisotropy across the contiguous U.S. determined by Rayleigh wave ellipticity. *Geophysical Research Letters*, *41*(23), 8301–8307. https://doi.org/10.1002/2014GL062362

Liu, H., Byrnes, J. S., Bezada, M., Wu, Q., Pei, S., & He, J. (2022). Variable depths of magma genesis in the North China craton and central asian Orogenic belt inferred from teleseismic P wave attenuation. *Journal of Geophysical Research: Solid Earth*, *127*(3), e2021JB022439. https://doi.org/10.1029/2021JB022439

Liu, K. H., Elsheikh, A., Lemnifi, A., Purevsuren, U., Ray, M., Refayee, H., et al. (2014). A uniform database of teleseismic shear wave splitting measurements for the western and central United States. *Geochemistry, Geophysics, Geosystems*, *15*(5), 2075–2085. https://doi.org/10.1002/2014GC005267

Long, M. D., Benoit, M. H., Evans, R. L., Aragon, J. C., & Elsenbeck, J. (2020). The MAGIC experiment: A combined seismic and magnetotelluric deployment to investigate the structure, dynamics, and evolution of the central Appalachians. *Seismological Research Letters*, *91*(5), 2960–2975. https://doi.org/10.1785/0220200150

Long, M. D., Jackson, K. G., & McNamara, J. F. (2016). SKS splitting beneath Transportable Array stations in eastern North America and the signature of past lithospheric deformation. *Geochemistry, Geophysics, Geosystems*, *17*(1), 2–15. https://doi.org/10.1002/2015GC006088

21699356, 2023, 12, Downloaded from https://agupubs.onlinelibrary.wiley.com/doi/10.1029/2023JB027299, Wiley Online Library on [11/12/2023]. See the Terms and Conditions (https://onlinelibrary.wiley.com/terms-and-conditions) on Wiley Online Library for rules of use; OA articles are governed by the applicable Creative Commons License

Long, M. D., Wagner, L. S., King, S. D., Evans, R. L., Mazza, S. E., Byrnes, J. S., et al. (2021). Evaluating models for lithospheric loss and intraplate volcanism beneath the central appalachian mountains. *Journal of Geophysical Research: Solid Earth*, *126*(10), e2021JB022571. https://doi.org/10.1029/2021JB022571

Malinverno, A., & Briggs, V. A. (2004). Expanded uncertainty quantification in inverse problems: Hierarchical Bayes and empirical Bayes. *Geophysics*, *69*(4), 1005–1016. https://doi.org/10.1190/1.1778243

Mazza, S. E., Gazel, E., Johnson, E. A., Bizimis, M., McAleer, R., & Biryol, C. B. (2017). Post-rift magmatic evolution of the eastern North American "passive-aggressive" margin. *Geochemistry, Geophysics, Geosystems*, *18*(1), 3–22. https://doi.org/10.1002/2016GC006646

Menke, W., Lamoureux, J., Abbott, D., Hopper, E., Hutson, D., & Marrero, A. (2018). Crustal heating and lithospheric alteration and erosion associated with asthenospheric upwelling beneath southern New England (USA). *Journal of Geophysical Research: Solid Earth*, *123*(10), 8995–9008. https://doi.org/10.1029/2018JB015921

Menke, W., Skryzalin, P., Levin, V., Harper, T., Darbyshire, F., & Dong, T. (2016). The Northern appalachian anomaly: A modern asthenospheric upwelling. *Geophysical Research Letters*, *43*(19), 10173–10179. https://doi.org/10.1002/2016GL070918

Mittal, V., Long, M. D., Evans, R. L., Byrnes, J. S., & Bezada, M. (2023). Joint analysis of seismic and electrical observables beneath the central Appalachians requires partial melt in the upper mantle. *Geochemistry, Geophysics, Geosystems*, *24*(3), e2022GC010690. https://doi.org/10.1029/2022GC010690

Oliveira, R., & Bezada, M. (2022). The Yellowstone paradox: A decoupling of seismic velocity and attenuation. In *Presented at the AGU fall meeting* (Vol. 2022, p. DI25C-0042).

Pang, G., Abers, G. A., & van Keken, P. E. (2023). Focusing effects of teleseismic wavefields by the subducting plate beneath cascadia. *Journal of Geophysical Research: Solid Earth*, *128*(6), e2022JB025486. https://doi.org/10.1029/2022JB025486

Pasyanos, M. E., Masters, T. G., Laske, G., & Ma, Z. (2014). LITHO1.0: An updated crust and lithospheric model of the Earth. *Journal of Geophysical Research: Solid Earth*, *119*(3), 2153–2173. https://doi.org/10.1002/2013JB010626

Pavlis, G. L., Sigloch, K., Burdick, S., Fouch, M. J., & Vernon, F. L. (2012). Unraveling the geometry of the Farallon plate: Synthesis of three-dimensional imaging results from USArray. *Tectonophysics*, *532–535*, 82–102. https://doi.org/10.1016/j.tecto.2012.02.008

Porritt, R. W., Becker, T. W., Boschi, L., & Auer, L. (2021). Multiscale, radially anisotropic shear wave imaging of the mantle underneath the contiguous United States through joint inversion of USArray and global data sets. *Geophysical Journal International*, *226*(3), 1730–1746. https://doi.org/10.1093/gji/ggab185

Porter, R., Liu, Y., & Holt, W. E. (2016). Lithospheric records of orogeny within the continental U.S. *Geophysical Research Letters*, *43*(1), 144–153. https://doi.org/10.1002/2015GL066950

Porter, R. C., van der Lee, S., & Whitmeyer, S. J. (2019). Synthesizing EarthScope data to constrain the thermal evolution of the continental U.S. lithosphere. *Geosphere*, *15*(6), 1722–1737. https://doi.org/10.1130/GES02000.1

Romanowicz, B. A., & Mitchell, B. J. (2015). 1.25—Deep Earth structure: Q of the Earth from crust to core. In G. Schubert (Ed.), *Treatise on geophysics* (2nd ed., pp. 789–827). Elsevier. https://doi.org/10.1016/B978-0-444-53802-4.00021-X

Schmandt, B., & Lin, F.-C. (2014). P and S wave tomography of the mantle beneath the United States. *Geophysical Research Letters*, *41*(18), 2014GL061231. https://doi.org/10.1002/2014GL061231

Schulte-Pelkum, V., & Mahan, K. H. (2014). A method for mapping crustal deformation and anisotropy with receiver functions and first results from USArray. *Earth and Planetary Science Letters*, *402*, 221–233. https://doi.org/10.1016/j.epsl.2014.01.050

Shen, W., & Ritzwoller, M. H. (2016). Crustal and uppermost mantle structure beneath the United States. *Journal of Geophysical Research: Solid Earth*, *121*(6), 2016JB012887. https://doi.org/10.1002/2016JB012887

Smith, R. B., Jordan, M., Steinberger, B., Puskas, C. M., Farrell, J., Waite, G. P., et al. (2009). Geodynamics of the Yellowstone hotspot and mantle plume: Seismic and GPS imaging, kinematics, and mantle flow. *Journal of Volcanology and Geothermal Research*, *188*(1), 26–56. https://doi.org/10.1016/j.jvolgeores.2009.08.020

Smith, R. B., & Siegel, L. J. (2000). *Windows into the Earth: The geologic story of Yellowstone and Grand Teton National Parks*. Oxford University Press.

Soto Castaneda, R. A. S., Abers, G. A., Eilon, Z. C., & Christensen, D. H. (2021). Teleseismic attenuation, temperature, and melt of the upper mantle in the Alaska subduction zone. *Journal of Geophysical Research: Solid Earth*, *126*(7), e2021JB021653. https://doi.org/10.1029/2021JB021653

Stanciu, A. C., & Humphreys, E. D. (2020). Upper mantle tomography beneath the Pacific Northwest interior. *Earth and Planetary Science Letters*, *539*, 116214. https://doi.org/10.1016/j.epsl.2020.116214

Tasaka, M., & Hiraga, T. (2013). Influence of mineral fraction on the rheological properties of forsterite + enstatite during grain-size-sensitive creep: 1. Grain size and grain growth laws. *Journal of Geophysical Research: Solid Earth*, *118*(8), 3970–3990. https://doi.org/10.1002/jgrb.50285

Teng, T.-L. (1968). Attenuation of body waves and the Q structure of the mantle. *Journal of Geophysical Research*, *73*(6), 2195–2208. https://doi.org/10.1029/JB073i006p02195

VanderBeek, B. P., Bue, R. L., Rappisi, F., & Faccenda, M. (2023). Imaging upper mantle anisotropy with travel-time and splitting intensity observations from teleseismic shear waves: Insights from tomographic reconstructions of subduction simulations. *Geophysical Journal International*, *235*(3), 2670. https://doi.org/10.1093/gji/ggad389

VanderBeek, B. P., & Faccenda, M. (2021). Imaging upper mantle anisotropy with teleseismic P-wave delays: Insights from tomographic reconstructions of subduction simulations. *Geophysical Journal International*, *225*(3), 2097–2119. https://doi.org/10.1093/gji/ggab081

Wei, S. S., & Wiens, D. A. (2018). P-wave attenuation structure of the Lau back-arc basin and implications for mantle wedge processes. *Earth and Planetary Science Letters*, *502*, 187–199. https://doi.org/10.1016/j.epsl.2018.09.005

Wei, S. S., & Wiens, D. A. (2020). High bulk and shear attenuation due to partial melt in the Tonga-lau back-arc mantle. *Journal of Geophysical Research: Solid Earth*, *125*(1), e2019JB017527. https://doi.org/10.1029/2019JB017527

Whitmeyer, S. J., & Karlstrom, K. E. (2007). Tectonic model for the proterozoic growth of North America. *Geosphere*, *3*(4), 220–259. https://doi.org/10.1130/GES00055.1

Worthington, L. L., Miller, K. C., Erslev, E. A., Anderson, M. L., Chamberlain, K. R., Sheehan, A. F., et al. (2016). Crustal structure of the Bighorn Mountains region: Precambrian influence on Laramide shortening and uplift in north-central Wyoming. *Tectonics*, *35*(1), 2015TC003840. https://doi.org/10.1002/2015TC003840

Yamauchi, H., & Takei, Y. (2016). Polycrystal anelasticity at near-solidus temperatures. *Journal of Geophysical Research: Solid Earth*, *121*(11), 7790–7820. https://doi.org/10.1002/2016JB013316

Zhou, T., Li, J., Xi, Z., Li, G., & Chen, M. (2022). CUSRA2021: A radially anisotropic model of the contiguous US and surrounding regions by full-waveform inversion. *Journal of Geophysical Research: Solid Earth*, *127*(8), e2021JB023893. https://doi.org/10.1029/2021JB023893

Zhu, Z., Bezada, M. J., Byrnes, J. S., & Ford, H. A. (2021). Evidence for stress localization caused by lithospheric heterogeneity from seismic attenuation. *Geochemistry, Geophysics, Geosystems*, *22*(11), e2021GC009987. https://doi.org/10.1029/2021GC009987

21699356, 2023, 12, Downloaded from https://agupubs.onlinelibrary.wiley.com/doi/10.1029/2023JB027299, Wiley Online Library on [11/12/2023]. See the Terms and Conditions (https://onlinelibrary.wiley.com/terms-and-conditions) on Wiley Online Library for rules of use; OA articles are governed by the applicable Creative Commons License